



Published in final edited form as:

Cell Rep. 2021 November 23; 37(8): 110055. doi:10.1016/j.celrep.2021.110055.

## A renal cell carcinoma tumorgraft platform to advance precision medicine

**Roy Elias<sup>1,2,12,13</sup>, Vanina T. Tcheuyap<sup>1,12</sup>, Akash K. Kaushik<sup>3</sup>, Nirmish Singla<sup>1,4,14</sup>, Ming Gao<sup>1</sup>, Oscar Reig Torras<sup>1,15</sup>, Alana Christie<sup>1,5</sup>, Aditi Mulgaonkar<sup>6</sup>, Layton Woolford<sup>1</sup>, Christina Stevens<sup>1</sup>, Kavitha Priya Kettimuthu<sup>7</sup>, Andrea Pavia-Jimenez<sup>1</sup>, Lindsey K. Boroughs<sup>3,16</sup>, Allison Joyce<sup>1</sup>, Marianna Dakanali<sup>6</sup>, Hollis Notgrass<sup>8</sup>, Vitaly Margulis<sup>1,4</sup>, Jeffrey A. Cadeddu<sup>1,4</sup>, Ivan Pedrosa<sup>1,6,9</sup>, Noelle S. Williams<sup>1,10</sup>, Xiankai Sun<sup>1,6,9</sup>, Ralph J. DeBerardinis<sup>1,3</sup>, Orhan K. Öz<sup>1,6</sup>, Hua Zhong<sup>8,10</sup>, Somasekar Seshagiri<sup>11,17</sup>, Zora Modrusan<sup>11</sup>, Brandi L. Cantarel<sup>10</sup>, Payal Kapur<sup>1,4,8</sup>, James Brugarolas<sup>1,2,18,\*</sup>**

<sup>1</sup>Kidney Cancer Program, Simmons Comprehensive Cancer Center, The University of Texas Southwestern Medical Center, Dallas, TX, USA

<sup>2</sup>Department of Internal Medicine, The University of Texas Southwestern Medical Center, Dallas, TX, USA

<sup>3</sup>Howard Hughes Medical Institute and Children's Medical Center Research Institute, University of Texas Southwestern Medical Center, Dallas, TX, USA

<sup>4</sup>Department of Urology, The University of Texas Southwestern Medical Center, Dallas, TX, USA

<sup>5</sup>Division of Biostatistics, Department of Clinical Sciences, The University of Texas Southwestern Medical Center, Dallas, TX, USA

<sup>6</sup>Department of Radiology, The University of Texas Southwestern Medical Center, Dallas, TX, USA

<sup>7</sup>Department of Biochemistry, The University of Texas Southwestern Medical Center, Dallas, TX, USA

<sup>8</sup>Department of Pathology, The University of Texas Southwestern Medical Center, Dallas, TX, USA

<sup>9</sup>Advanced Imaging Research Center, The University of Texas Southwestern Medical Center, Dallas, TX, USA

This is an open access article under the CC BY-NC-ND license (<http://creativecommons.org/licenses/by-nc-nd/4.0/>).

\*Correspondence: james.brugarolas@utsw.edu.

### AUTHOR CONTRIBUTIONS

Conceptualization, R.E., P.K., and J.B.; TG model acquisition, V.T.T., L.W., C.S., A.P.-J., A.J., H.N., P.K., and J.B.; genomic/transcriptomic analysis, R.E., O.R.T., H.Z., S.S., Z.M., B.L.C., and J.B.; metabolomics, L.K.B., A.K.K., and R.J.D.; immunoPET, A.M., M.D., X.S., O.K.Ö., I.P., and J.B.; pharmacokinetics, V.T.T., K.P.K., N.S.W., M.G., and J.B.; drug trials: V.T.T., M.G., and J.B.; data curation, R.E., V.T.T., A.K.K., N.S., A.C., A.M., L.W., C.S., A.P.-J., N.S.W., X.S., R.J.D., O.K.Ö., H.Z., S.S., Z.M., B.L.C., P.K., and J.B.; writing – original draft: R.E. and N.S.; writing – review & editing, V.T.T., A.K.K., C.S., I.P., N.S.W., X.S., R.J.D., O.K.Ö., H.Z., S.S., Z.M., B.L.C., P.K., and J.B.; visualization, R.E., A.C., and A.K.K.; resources, R.E., V.T.T., L.W., C.S., A.P.-J., A.J., V.M., J.A.C., I.P., N.S.W., X.S., R.J.D., O.K.Ö., H.Z., B.L.C., S.S., Z.M., P.K., and J.B.; supervision, I.P., N.S.W., X.S., R.J.D., O.K.Ö., H.Z., B.L.C., P.K., and J.B.; funding acquisition, J.B.

### SUPPLEMENTAL INFORMATION

Supplemental information can be found online at <https://doi.org/10.1016/j.celrep.2021.110055>.

<sup>10</sup>Department of Bioinformatics, The University of Texas Southwestern Medical Center, Dallas, TX, USA

<sup>11</sup>Department of Microchemistry, Proteomics, Lipidomics and NGS, Genentech, Inc., South San Francisco, CA, USA

<sup>12</sup>These authors contributed equally

<sup>13</sup>Present address: Sidney Kimmel Comprehensive Cancer Center, Johns Hopkins University School of Medicine, 401 N. Broadway, Baltimore, MD 21231, USA

<sup>14</sup>Present address: Departments of Urology and Oncology, The James Buchanan Brady Urological Institute, Johns Hopkins University School of Medicine, 600 N. Wolfe St., Baltimore, MD 21287, USA

<sup>15</sup>Present address: Department of Oncology, Hospital Clinic de Barcelona and Translational Genomic and Targeted Therapeutics in Solid Tumors, Institut d'Investigacions Biomèdiques August Pi i Sunyer (IDIBAPS), C/ Villarroel 170, Barcelona, Spain

<sup>16</sup>Present address: Bristol-Myers Squibb, 4931 George Rd, Tampa, FL 33634, USA

<sup>17</sup>Present address: SciGenom Research Foundation, Bangalore, Karnataka, India

<sup>18</sup>Lead contact

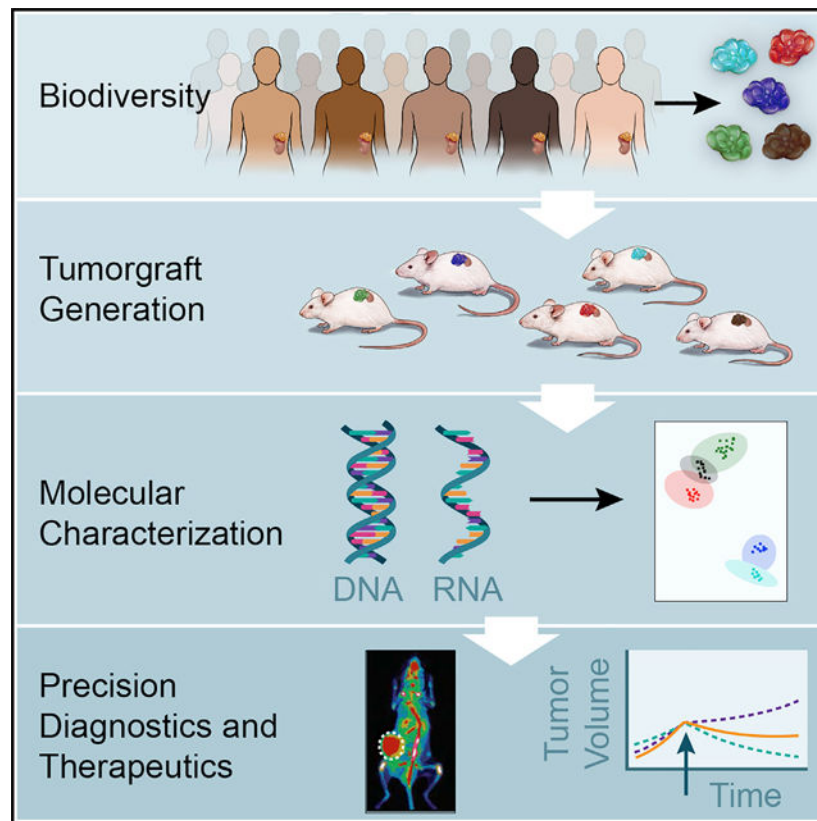
## SUMMARY

Renal cell carcinoma (RCC) encompasses a heterogeneous group of tumors, but representative preclinical models are lacking. We previously showed that patient-derived tumorgraft (TG) models recapitulate the biology and treatment responsiveness. Through systematic orthotopic implantation of tumor samples from 926 ethnically diverse individuals into non-obese diabetic (NOD)/severe combined immunodeficiency (SCID) mice, we generate a resource comprising 172 independently derived, stably engrafted TG lines from 148 individuals. TG lines are characterized histologically and genomically (whole-exome [ $n = 97$ ] and RNA [ $n = 102$ ] sequencing). The platform features a variety of histological and oncogenotypes, including TCGA clades further corroborated through orthogonal metabolomic analyses. We illustrate how it enables a deeper understanding of RCC biology; enables the development of tissue- and imaging-based molecular probes; and supports advances in drug development.

## In brief

Elias et al. report a renal cell carcinoma (RCC) tumorgraft (TG) resource from 926 ethnically diverse individuals at the UT Southwestern Kidney Cancer Program whose tumors were implanted orthotopically into immunodeficient mice and characterized through next-generation sequencing. Potential applications are discussed, including examples in areas such as molecular imaging and precision therapy.

## Graphical Abstract



## INTRODUCTION

Approximately 430,000 new cases of renal cell carcinoma (RCC) are diagnosed annually, and ~180,000 deaths occur worldwide (Sung et al., 2021). Current frontline regimens yield initial responses in up to 70% of individuals (Motzer et al., 2019, 2021; Choueiri et al., 2020, 2021; Powles et al., 2020). However, the disease ultimately progresses in the majority of individuals (Motzer et al., 2019; Choueiri et al., 2020; Powles et al., 2020). A major challenge is disease heterogeneity. The World Health Organization classifies RCC into 16 entities (Moch et al., 2016), but next-generation sequencing has revealed even greater molecular heterogeneity (Durinck et al., 2015; Chen et al., 2016a; Ricketts et al., 2018; Motzer et al., 2020a, 2020b).

Tumorgraft (TG) models, which involve implantation of tumor samples from affected individuals into immunocompromised mice, enable studies in a physiological context (Sobczuk et al., 2020). RCC TGs reproduce the histology, gene expression, DNA copy number alterations, and mutations of the corresponding tumors from affected individuals (Sivanand et al., 2012; Pavía-Jiménez et al., 2014; Grisanzio et al., 2011). In addition, RCC TGs preserve the drug responsiveness of human RCC (Sivanand et al., 2012; Chen et al., 2016b; Karam et al., 2011; Ingels et al., 2014; Cho et al., 2016; Zhao et al., 2017; Elbanna et al., 2020; Moserle et al., 2020). In studies optimizing drug administration regimens to model human exposures, RCC TGs have been shown to respond to sunitinib (Motzer et al., 2009; Bukowski et al., 2007), but not to erlotinib, used as a negative

control (Sivanand et al., 2012). TGs also respond to rapamycin (also called sirolimus), the dominant active metabolite of temsirolimus, which is largely a sirolimus prodrug (Ingels et al., 2014; Sivanand et al., 2012; Brugarolas et al., 2008). Thus, based on these results, RCC TGs appear to respond to the two main classes of RCC targeted therapies: inhibitors of angiogenesis and rapalogs. More recently, we found that clear cell RCC (ccRCC) TGs respond to the HIF-2 $\alpha$  inhibitor PT2399 (Chen et al., 2016b), and similar results were subsequently observed in clinical trials (Courtney et al., 2018b; Jonasch et al., 2019).

Building on our previous work (PeñLlopis et al., 2012; Sivaand et al., 2012; Chen et al., 2016b; Wolff et al., 2015; Wang et al., 2018; Vento et al., 2019; Singla et al., 2020) and expanding on reports from other groups (Grisanzio et al., 2011; Karam et al., 2011; Varna et al., 2014; Cho et al., 2016; Zhao et al., 2017; Elbanna et al., 2020; Moserle et al., 2020), we present a most comprehensive resource in its extent and breadth of applications.

## RESULTS

### Resource development

Between January 1, 2008 and December 31, 2019, 1,235 samples originating from 926 individuals at UT Southwestern Medical Center (UTSW) and the affiliated county hospital (Parkland Health and Hospital System) who gave consent for tissue-based research were implanted into mice, creating the UTSW Kidney Cancer Program (KCP) TG platform (Figure 1). Individuals with a presumed diagnosis of RCC were eligible. Of the 1,235 implanted samples, 1,067 were from localized or regionally advanced disease (primary tumor and regional lymph nodes) and 168 from distant metastases. Primary tumors were prioritized based on aggressiveness (STAR Methods). Tumor fragments were implanted orthotopically without disaggregation or additives, into non-obese diabetic (NOD)/severe combined immunodeficiency (SCID) mice (Pavía-Jimeénez et al., 2014). Although xenotransplantation tends to select for aggressive tumors (Sivanand et al., 2012), our updated resource includes 172 stably engrafted (successfully passaged through at least two cohorts of mice) TG lines corresponding to 148 individuals (Figure 1).

TG lines were derived from an ethnically and racially diverse group of individuals (Figure 2A). The median patient age at implantation was 60 years (ranging from 24–87), and the male to female ratio was ~2:1 (Table S1). RCC has the ability to directly extend into the renal vein, forming a “tumor thrombus,” which was the origin for 28 (16.3%) lines. Eight (4.7%) lines were derived from regional lymph node metastases and 31 (18.0%) from distant metastatic sites. Common (lung, liver, and bone) as well as less frequent (pancreas, spinal cord, and testis) sites are represented (Table S2).

RCC exhibits intratumoral and intra-individual heterogeneity (Turajlic et al., 2018a, 2018b; Gerlinger et al., 2012, 2014). Our library contains 46 lines from 22 individuals, including 34 lines from multiregional sampling of primary tumor, tumor thrombus, and regional lymph nodes, as well as 12 lines from metachronous primary and metastasis sites (Table S3). A nomenclature key and detailed clinicopathologic characteristics are shown in Tables S4 and S5, respectively.

## The KCP TG library captures histologically defined ccRCC and non-ccRCC (nccRCC) subtypes

Among RCC, ccRCC accounts for ~75% of cases. Accordingly, the majority of TG lines ( $n = 136$ , 79%) are ccRCCs (Figure 2B). ccRCC is further subdivided by nuclear grade and sarcomatoid and/or rhabdoid dedifferentiation. Table S6 provides comprehensive histological annotation. Although the majority of ccRCC lines were of high grade, 9 were of low grade (ISUP 2). Fifteen TG lines represented subclones with varying nuclear grades (Table S6). ccRCC can be further subdivided on the basis of cytology, architecture, and stroma (Cai et al., 2020), and engrafted TGs often recapitulated the architecture of parent tumors (Figure 2C).

nccRCC subtypes (Moch et al., 2016) exhibit unique histological and molecular features (Durinck et al., 2015; Cancer Genome Atlas Research Network et al., 2016; Linehan et al., 2016; Davis et al., 2014). Our platform contains 36 (20.9%) nccRCC lines, including 9 papillary RCCs (pRCCs) and 16 unclassified RCCs (uRCCs) (Figure 2B). Rarer subtypes, including MiT family translocation RCC (tRCC) ( $n = 7$ ), and fumarate hydratase (FH)-deficient RCC ( $n = 4$ ), have also been established. Histologic features were preserved in paired TGs (Figure 2D). However, no chromophobe RCC (chRCC) TG lines could be generated despite implantation of 54 chRCC tumors. This may reflect the more indolent biology of chRCC (Vera-Badillo et al., 2012). However, given that aggressive chRCC tumors (i.e., with sarcomatoid elements) similarly failed to engraft, there may be fundamental differences between chRCC and other subtypes in their ability to engraft or thrive as TGs.

Sarcomatoid dedifferentiation is prognostic and potentially predictive (Bi et al., 2016; Bakouny et al., 2021; Tannir et al., 2021), and sarcomatoid features were identified in 16 TG lines. Rhabdoid features were found in 17 lines. Simultaneous sarcomatoid and rhabdoid dedifferentiation was identified in 6 lines (Table S6). Additionally, there were several lines in which tumor fragments engrafted with and without sarcomatoid ( $n = 9$  TG lines) or rhabdoid ( $n = 8$  TG lines) features.

## Frequent drivers and rare mutations represented in the TG library

Whole-exome sequencing (WES) was performed on 125 fresh-frozen TG specimens derived from 97 (56.4%) TG lines (Table S7). In comparison with parent tumors (106 TG samples corresponding to 103 samples from affected individuals), 88% (interquartile range [IQR], 81%–94%) of somatic mutations identified were detected in corresponding TGs (Figure S1A). Because the stroma is replaced by the mouse (Hahn et al., 1995), TGs offer greater sensitivity for mutation detection (in humans, DNA from tumor cells is diluted by DNA from stromal cells) (Peña-Llopis et al., 2012). The median mutant allele frequency (MAF) was 0.24 (IQR, 0.18–0.49) in tumors from affected individuals versus 0.44 (0.39–0.47,  $p = 7.4e-14$ ) in TGs (Figures S1B and S1C). Higher MAFs may also reflect less intratumoral heterogeneity, and, not unexpectedly, TG analyses enabled detection of a greater number of mutations. Although the median tumor mutation burden (TMB) in tumors from affected individuals was 30.3 (IQR, 25.1–38.9), it rose to 49.1 (IQR, 45–56.9,  $p = 6.5e-13$ ) in TGs. A possible confounding factor is mutation acquisition with TG passage over time. WES data from 15 TG lines with at least 2 cohorts of mice ( $n = 36$  samples, ranging from cohort 0

[c0]–c13) were analyzed (Figure S1D). The biggest differences in mutation numbers were observed between c0 and c1, which, we speculate, may reflect stroma replacement and possibly clonal outgrowth. Subsequently, TMB remained fairly constant.

Canonical driver mutations were identified with similar frequencies as in affected individuals (Cancer Genome Atlas Research Network, 2013; Peña-Llopis et al., 2012; Durinck et al., 2015; Linehan et al., 2016; Davis et al., 2014; Chen et al., 2016c), albeit with increased representation of mutations associated with aggressiveness. Summary statistics are provided on a per-individual level (n = 84). For ccRCC (n = 65 individuals), they included mutations in *VHL* (n = 52, 80%), *PBRM1* (n = 28, 43.1%), *SETD2* (n = 21, 32.3%), *BAP1* (n = 13, 20%), *TP53* (n = 8, 12.3%), and *PTEN* (n = 7, 10.8%) (Figure 3A). Other less frequently mutated drivers included the chromatin remodeling genes *KDM5C* (n = 8, 12.3%), *KMT2C* (n = 5, 7.7%), *ARID1B* (n = 4, 6.2%), *KMT2D* (n = 3, 4.6%), and *ARID1A* (n = 1, 1.5%); the mTOR pathway genes *MTOR* (n = 7, 10.8%), *TSC1* (n = 5, 7.7%), and *TSC2* (n = 2, 3.1%); as well as *NF2* (n = 4, 6.2%), *NFI* (n = 3, 4.6%), and *HIF1A* (n = 3, 4.6%). One TG line, XP483, had a homozygous nonsense mutation (MAF, ~1) in the mismatch repair gene *MLH1* (XP483Tc\_TGc0 and XP483Td\_TGc0; Table S7). Interestingly, the TMB of these samples far exceeded the median (691 versus 49.1) and may reflect a unique subtype of ccRCC (Figure 3A).

WES was performed on 24 nccRCC TG lines (34 samples), including 10 uRCC, 6 tRCC, 5 pRCC, and 3 FH-deficient RCC lines (derived from 19 individuals) (Figure 3B). Although numbers are limited, mutations in key genes included *TP53* (n = 3, 15.8%) and *SETD2* (n = 3, 15.8%); the Hippo pathway genes *FAT1*, *FAT4*, and *NF2*; the SWI/SNF complex genes *PBRM1*, *ARID1A*, and *ARID1B*; the mTOR pathway genes *PTEN* and *TSC2*; as well as regulators of the NRF2/ARE pathway *KEAP1* and *CUL3*. *FH* mutations were identified in 3 tumors, including one TG from an individual with a germline *FH* mutation. Fusion analysis (manuscript in preparation) of RNA sequencing (RNA-seq) data for tRCC samples revealed translocations involving *TFEB* (n = 2, 10.5%) and *TFE3* (n = 4, 21.1%). All putative somatic mutations are shown in Table S8.

### Integrated transcriptomic profiling identifies major molecular subtypes

We performed RNA-seq on 131 TG specimens from 102 lines (Table S7). A comparison of TG transcriptomes with the corresponding tumors from affected individuals (n = 132 samples) and normal samples (n = 58) using principal-component analysis (PCA) of the top 25% most variable genes (by coefficient of variation, n = 9,900) revealed three distinct groups (Figure S2A). This is consistent with the notion that TGs and corresponding tumors differ by human versus murine stroma and that transcripts from the latter are removed. We previously leveraged this feature to empirically define a gene set corresponding to the tumor microenvironment (n = 2,080 genes) (Wang et al., 2018). This empirically defined tumor microenvironment (eTME) gene set led to identification of two pan-RCC clades: inflamed and non-inflamed (Wang et al., 2018). We removed eTME genes from the top 25% most variably expressed genes (n = 430) (Figure S2A) and performed unsupervised hierarchical clustering of TGs (n = 116) and corresponding tumors from affected individuals (n = 121). This analysis correctly paired TG samples with the corresponding tumors from affected

individuals in 82.7% of cases (96 of 116) (Figure S2B). Successfully paired TGs included tumors from late passages up to cohort 16.

Transcriptomic profiling of RCC has revealed substantial molecular heterogeneity (Chen et al., 2016a; Brannon et al., 2010; Cancer Genome Atlas Research Network, 2013; Motzer et al., 2020a). We merged RNA-seq from our TGs (n = 131 samples) with The Cancer Genome Atlas (TCGA) Pan-Kidney (KIPAN) dataset, consisting of 894 RCC tumors of different histologies. Chen et al. (2016a) previously defined 9 subgroups through multi-omics analysis and generated an 800-gene signature that distinguishes these subtypes. Of the 9 defined subgroups, 3 were enriched for ccRCC (CC-e.1–3), and 4 for pRCC (P-e1.a/b, P-e.2, and P.CIMP-e). The subgroups were biologically distinct and had prognostic implications (worse survival in CCe.3 and P.CIMP-e) (Chen et al., 2016a). To explore these transcriptomic subgroups, we subtracted 124 genes overlapping with the eTME signature (Wang et al., 2018) from the 800-gene list, leaving 676 genes according to which TCGA and TG samples were analyzed using Uniform Manifold Approximation and Projection (UMAP) (Figure 4; STAR Methods). For an interactive and searchable version, see Data S1. These analyses revealed a good separation between TCGA ccRCC (CC-e.1–3) and pRCC (P-e1.a/b, P-e.2, and P.CIMP-e), but the distinction among subtypes was less clear. However, TGs could be identified corresponding to all 7 molecular subgroups. Compared with the corresponding UTSW cohort, TG samples revealed a relative expansion of the aggressive CC-e.1 clade, but this was not statistically significant (Figure S3A; Chen et al., 2016a). This is consistent with the notion that engraftment in mice selects for aggressive tumors (Sivanand et al., 2012). tRCC TG lines tended to make their own cluster reflecting unique biology. They were close to pRCC and included a disproportionate number of uRCC. Consistent with the unsupervised clustering analyses, samples from the same individuals tended to cluster together.

We assessed the concordance of predicted “KIPAN clusters” between paired parent tumors (n = 121) and corresponding TGs (n = 116) (STAR Methods). Among TG samples that could be assigned a cluster, 78 of 106 (74%) were predicted to fall within the same cluster as their corresponding parent tumor (Figure S3B). Samples that failed to cluster with parent tumors may represent examples of intratumoral heterogeneity. Notably, despite limited numbers, there was a strong correlation between the predicted tumor clusters from affected individuals and overall survival (OS). As expected, CC-e.3 and CC-e.1 had shorter OS relative to the CC-e.2 (Figure S3C).

### Application 1: Exploring and probing metabolism

ccRCC is characterized by altered metabolism, which is influenced by underlying driver mutations. Frequent loss of *VHL* and subsequent alterations in hypoxia-related genes induce the Warburg effect (Hakimi et al., 2016; Courtney et al., 2018a; DiNatale et al., 2020), but other abnormalities likely contribute as well. We generated metabolic profiles of 134 ccRCC TG samples from 16 TG lines: CC-e.1 (n = 7), CC-e.2 (n = 3), and CC-e.3 (n = 6). A total of 119 metabolites were analyzed using liquid-chromatography-mass spectrometry (LC/MS). Partial least-squares discriminant analysis (PLS-DA) revealed 3 clusters (Figure S4). We generated a heatmap of the 50 most variable metabolites (Figure 5A; samples arranged by

unsupervised clustering). Metabolic analyses separated CC-e.3 relative to CC-e.1/2. CC-e.3 was characterized by a significant increase in pyruvate, lactate, and glucose/fructose (which were indistinguishable) and a relative decrease of aspartate. These data suggest enhanced glycolysis and reduced oxidative metabolism in CC-e.3 tumors. Additionally, cystathionine, an intermediate of glutathione (GSH) metabolism, was proportionally enriched in CC-e.3 (Figure 5B). These data suggest that metabolism is rewired to support aggressive tumor growth (Chen et al., 2016a; Hakimi et al., 2016). Thus, TG models can be used to probe differences in metabolism and to develop therapeutic interventions aiming at metabolic pathways.

## Application 2: Precision diagnostics

Given the similarities between TGs and corresponding tumors, TGs may be suited to advance diagnostics (tissue- and imaging-based). Of particular interest to us is development of molecular imaging probes. The PD-L1/PD-1 axis is the most exploited to date for immunotherapy (Sharma and Allison, 2020). PD-L1, an immune checkpoint protein expressed on the surface of tumors and other cells, is predictive of responsiveness to PD-L1/PD-1 targeting drugs in multiple tumor types but not in RCC (Davis and Patel, 2019). This may be, at least in part, due to RCC heterogeneity, which may influence assessments based on limited material from tumor biopsies (or the use of archival samples). We developed a method for comprehensive, realtime, PD-L1 evaluation enabling dynamic assessment of interventions (i.e., radiotherapy, systemic treatments) and potentially changes associated with resistance acquisition. TGs were selected with high and low PD-L1 expression (Figures 6A and 6B), implanted in the flanks of mice, and evaluated by positron emission tomography (PET) using a zirconium-89 ( $^{89}\text{Zr}$ ) conjugated anti-PD-L1 antibody we generated (Vento et al., 2019). The antibody, atezolizumab (ATZ), has a mutant Fc fragment that increases its specificity. These studies (Figure 6C) provided key pharmacokinetic (PK) and pharmacodynamic (PD) information supporting an Investigator New Drug (IND) application (IND143266) and an ongoing clinical trial ([ClinicalTrials.gov: NCT04006522](https://clinicaltrials.gov/ct2/show/study/NCT04006522)). PET/computed tomography (CT) of a study participant is shown in Figure 6D. Substantial PD-L1 heterogeneity was observed that correlated with responsiveness to anti-PD-1/CTLA-4 combination therapy. This heterogeneity underscores the challenges of tissue-based PD-L1 analyses. The same  $^{89}\text{Zr}$  conjugation process can be adapted to other antibodies. In addition, the same platform may be used to evaluate other molecular probes. As an example, we have developed a probe for HIF-2 $\alpha$  by adapting a first-in-class inhibitor (PT2385). Generated by Peloton Therapeutics in the UTSW BioCenter from UTSW chemical leads, PT2385 is highly specific for HIF-2 $\alpha$  (Scheuermann et al., 2009, 2013; Wallace et al., 2016; Chen et al., 2016b; Courtney et al., 2018b, 2020). By substituting a native F atom for  $^{18}\text{F}$ , we generated [ $^{18}\text{F}$ ]PT2385, which we evaluated using TGs with variable levels of HIF-2 $\alpha$  supporting an IND (IND156933) and a second ongoing clinical trial ([ClinicalTrials.gov: NCT04989959](https://clinicaltrials.gov/ct2/show/study/NCT04989959)). PT2385 is very similar to PT2977 (also called belzutifan), which the US Food and Drug Administration (FDA) recently approved for von Hippel-Lindau-associated tumors, including ccRCC. We speculate that [ $^{18}\text{F}$ ]PT2385 PET may help identify tumors most likely to respond to HIF-2 $\alpha$ -directed therapies.

### Application 3: Precision therapy

Mutations in the *BAP1* tumor suppressor gene are associated with aggressive ccRCC, and there is a need for new therapies (Peña-Llopis et al., 2012; Kapur et al., 2013, 2014). *BAP1* encodes a deubiquitinase (de Cubas and Rathmell, 2018). BAP1 deubiquitinates H2AK119Ub, regulating chromatin packing and gene expression (Scheuermann et al., 2010; Foglizzo et al., 2018). BAP1 catalytic activity is required for its tumor suppressor function (Peña-Llopis et al., 2012; Forbes et al., 2017; de Cubas and Rathmell, 2018). As a tumor suppressor protein, BAP1 is not targetable, but we reasoned that *BAP1* deficiency may increase sensitivity to drugs targeting the ubiquitin conjugation cascade. In mammals, ubiquitin conjugation is initiated by the E1 ubiquitin-activating enzyme (UAE), which is estimated to charge more than 99% of ubiquitin (Jin et al., 2007). Recently, a UAE inhibitor was reported, TAK-243 (MLN7243) (Hyer et al., 2018). TAK-243 has been shown to broadly inhibit protein ubiquitination and induce proteotoxic stress (Hyer et al., 2018). We hypothesized that BAP1-deficient tumors may be particularly sensitive to TAK-243 (Figure 7A).

To optimize TAK-243 administration to NOD/SCID mice, we performed PK analyses. We evaluated TAK-243 at 25 mg/kg intravenously (i.v.), which was the maximal dose reported (Hyer et al., 2018). In plasma, peak concentration ( $C_{max}$ ) was significantly lower than in humans (NCT02045095), but the area under the curve until last measurement ( $AUC_{last}$ ) was substantially higher. As in other tumor types (Hyer et al., 2018), TAK-243 accumulated in RCC tumors (Figure 7B; Table S10). TAK-243 suppressed H2AK119Ub in a BAP1-deficient (by immunohistochemistry [IHC]) RCC TG line (Figure 7C). We evaluated TAK-243 on mice implanted with two *BAP1*-deficient TG lines (XP258 and XP373). Unfortunately, TAK-243 did not affect tumor growth despite its effects on H2AK119Ub (Figure 7D; data not shown). The lack of activity was particularly troublesome because the plasma  $AUC_{last}$  in mice was ~8 times higher than in humans at the maximal tolerated dose in the phase 1 clinical trial, where serious adverse events were observed in 50% of participants (Table S10). In addition, 50 mg/kg i.v. was too toxic in mice. Used as a positive control, rapamycin, which is the dominant metabolite of temsirolimus, an FDA-approved drug (Hudes et al., 2007; Brugarolas et al., 2008), suppressed tumor growth.

#### A resource for the scientific community

We make available our Specialized Program of Research Excellence (SPORE)-funded UTSW KCP TG library to the scientific community. Cryopreserved TG tissue, which can be reconstituted as described previously (Pavía-Jiménez et al., 2014), may be obtained by submitting a request to KCPAdmin@utsouthwestern.edu. TG revival success rates range from 40%–80%, depending on tumor growth rates and other factors. To assist investigators with selecting the appropriate TG line(s), extensive clinicopathologic annotation is provided (Table S5), including mouse-level histological review (Table S6). Genomic data are available for a subset of TG lines (Table S7) and includes putative somatic mutations (Table S8) and normalized expression data (Table S9). Finally, an interactive version of Figure 4 is also available (Data S1). Raw WES and RNA-seq files are provided for individuals, giving their consent through the European Genome-Phenome Archive EGA: EGAS00001005516.

## DISCUSSION

Here we describe a comprehensive ethnically and demographically diverse RCC TG library. Over more than a decade, we transplanted tumors from over 900 individuals and generated over 170 stable TG lines. These lines encompass significant diversity within ccRCC and nccRCC subtypes. TG lines harbor mutations in common drivers as well as in less common cancer genes. Compared with tumors from affected individuals from the TCGA (Chen et al., 2016a), they represent major transcriptomic clusters. We discuss three particular applications, one probing metabolic pathways and the other two in the areas of precision diagnostics and therapeutics. However, the potential applications of TGs are extensive.

With respect to molecular genetics, TGs enable a deeper understanding of the mutation landscape and hold clues regarding tumor evolution. Because the stroma is replaced by the host, TG analyses enable mutation characterization specifically in tumor cells. Coupled with the fact that TG lines are generated from small tumor areas, which tend to be uniform, TGs offer greater sensitivity for mutation detection and greater MAF accuracy (Peña-Llopis et al., 2012). Indeed, TG MAFs approximated 0.5, the value expected for heterozygous mutations. The heightened MAF accuracy facilitated tracing evolution. For instance, a MAF of 0.3 may indicate a mutation in an area of duplication, which, if found in the amplified DNA segment, is likely to have occurred after duplication (Peña-Llopis et al., 2012). Such approaches can be valuable to infer mutational event sequence (Mitchell et al., 2018).

In addition, TGs can be used to characterize the tumor stroma. They enabled the first empirically generated RCC TME gene expression signature (Wang et al., 2018). This led us to discover two pan-RCC TME types: an inflamed and an uninfamed type (Wang et al., 2018). Inflamed tumors were enriched for *BAP1* mutations, suggesting that inflammation is linked to genotype and specifically *BAP1*. Tumor-induced inflammation appears to extend beyond the TME, and we discovered an association between inflamed tumors with thrombocytosis and anemia (Wang et al., 2018), two indicators of systemic inflammatory conditions (Kawai and Akira, 2010). Thrombocytosis and anemia are used in clinical practice to evaluate RCC prognosis (Heng et al., 2009), and their link to an inflamed TME provided a potential explanation for why they may be associated with poor outcomes. The data suggest that inflamed tumors are more aggressive. It is also interesting that the TME gene signature can help discriminate among subtypes. Indeed, a significant subset of the TCGA KIPAN classifier are eTME genes (124 of 800 genes).

Identification of inflamed and uninfamed RCC subtypes may have implications beyond prognosis. Inflamed tumors may be associated with greater response to immune checkpoint inhibitors (ICIs). Recent data identified a link between *BAP1* loss and reactivation of human endogenous retroviruses, which could contribute to ICI responsiveness (Panda et al., 2018). Furthermore, sarcomatoid tumors, which exhibit higher sensitivity to ICIs (Tannir et al., 2021), are enriched in *BAP1* mutations (Bakouny et al., 2021). Conversely, uninfamed tumors may be characterized by resistance to ICIs (McDermott et al., 2018). Uninfamed tumors are enriched for angiogenesis markers (Wang et al., 2018) and may be more responsive to inhibitors of angiogenesis. This is the case for RCCs that metastasize to

the pancreas, which are enriched for *PBRM1* mutations and may be more responsive to angiogenesis inhibitors (Singla et al., 2020).

RCC TGs may also enable studies of metastasis tropism. RCC is known for a wide range of metastasis destinations, and several destinations are encompassed in our library. Furthermore, inasmuch as some TGs grow subcutaneously as well as orthotopically (Table S5) but others only orthotopically, TGs offer the opportunity to study tissue factors that influence engraftment. Along these lines, tumors with *PBRM1* mutations are able to engraft in the pancreas (Singla et al., 2020). Although the extent to which *PBRM1* mutations facilitate pancreatic engraftment remains to be determined, our studies across implantation sites (subcutaneous tissue, kidney, and pancreas) suggest that different organs may support engraftment to different extents. In-depth studies of tropism, however, may require strains other than NOD/SCID mice, where metastases do not routinely develop. Others have reported that TGs metastasize in more immunocompromised strains (Grisanzio et al., 2011; Moserle et al., 2020). If the pattern of metastases in individuals were reproducible in these strains, they would offer a relevant model to study metastasis tropism. More immunocompromised mouse strains (such as Rag2;  $\gamma$ c-deficient mice) may also enable higher engraftment rates, broadening the tumor repertoire.

One of the advantages of our TG program is its being supported by an institutional review board (IRB) protocol that allows preservation of links to corresponding affected individuals. Therefore, we were able to determine that TGs also reproduce paraneoplastic syndromes (Sivanand et al., 2012). Paraneoplastic hypercalcemia (Sivanand et al., 2012) as well as polycythemia (unpublished data) are preserved in TGs. In addition, inasmuch as some TGs induce weight loss in their hosts but others do not, TGs may offer an experimental system to dissect cancer-induced cachexia. Furthermore, species differences between the tumor and host could be exploited to isolate wasting factors/cytokines and to test interventions such as neutralizing antibodies.

By selecting for aggressive tumors able to thrive in a different organism, TGs may also enable studies of determinants of aggressive biology. Our TGs are enriched for alterations of aggressive disease, such as mutations in *BAP1*, mTOR pathway genes, and *TP53*. Comparative studies may be performed of engrafted and non-engrafted tumors to further elucidate novel biology. This question may be particularly relevant to small renal masses (SRMs). Most SRMs do not metastasize, justifying active surveillance approaches, but a small number do. However, how these SRMs differ is not well understood. Because engraftment selects for particularly aggressive tumors, the analyses of SRMs engrafting in mice may help identify and probe determinants of aggressiveness. Another setting where engraftment may prove particularly useful is in the characterization of low-grade tumors. Although the majority of tumors that engrafted were of high grade, a few low-grade tumors were identified, which could be used to identify determinants of aggressiveness.

Although distinct driver mutations contribute to the clinical variability observed within RCC, they do not fully account for it. This variability may be further captured through gene expression analyses (Ricketts et al., 2018; Clark et al., 2019; Durinck et al., 2015; Cancer Genome Atlas Research Network, 2013, 2016). We have developed approaches

enabling successful integration of human RCC subtypes with TGs by focusing on the tumor cell transcriptome. Merging our TG library transcriptomic signature with the corresponding signature in the TCGA dataset (Chen et al., 2016a) allowed identification of TG lines representative of unique human molecular subtypes. Although there was relative enrichment for aggressive subtypes, representative lines of all 7 pRCC and ccRCC molecular subgroups were identified.

TGs extend analyses of metabolite abundance (metabolomics) of samples from affected individuals. Inasmuch as TGs can be readily processed and are not subject to the delays associated with surgeries or other confounding variables (i.e., ischemia), they may more faithfully reproduce at least some aspects of RCC metabolism (Neumeister and Juhl, 2018). TGs also enable study of how tumors utilize particular nutrients. TG-bearing mice can be infused with stable isotope-labeled nutrients to determine pathway utilization (Jang et al., 2018). These studies can help prioritize tracers for subsequent analyses in affected individuals and may serve as fertile ground for testing metabolism-directed interventions in appropriate tumor clades.

Another application of TGs is in precision diagnosis. Tumors with differential target expression can be implanted simultaneously in mice, enabling direct assessment of tracer specificity and reducing confounding from analyses in different mice. TG-bearing mice enable dynamic analyses of radiotracer accumulation over time as well as comparative analyses with other organs. TGs therefore assist with identification of appropriate imaging protocols and optimal readouts for subsequent trials in humans. TGs can also assist with diagnostics by providing renewable tissue sources for IHC analyses. Today, the workhorse of pathology is still IHC. IHC studies demand antibodies with no cross-reactivity, and their validation is a challenge. Tools available in research labs, such as small interfering RNA (siRNA) or gene editing, have limited application in clinical pathology. Thus, pathologists often resort to tissues from organs not known to express the particular target protein. However, utilization of such tissues also undermines the intended goal because these tissues may similarly not express potentially cross-reactive proteins. Thus, TG samples with mutations leading to loss of expression of particular proteins can be instrumental in establishing the specificity of antibodies. In addition, TGs can be used to expand genomically characterized tumor samples that can replenish stocks and aid in IHC development or serve as controls for IHC runs. As an example, we leveraged this platform to validate an IHC test that can distinguish BAP1 mutant and wild-type tumors with high sensitivity and specificity (Peña-Llopis et al., 2012; Kapur et al., 2013). This has been shown to be prognostic and has led to incorporation of the test in our clinical laboratory improvement amendments (CLIA)-certified clinical pathology lab (Joseph et al., 2014; Kapur et al., 2014).

Our platform, which contains extensive clinical, histologic, genomic, and transcriptomic annotation, can be utilized to identify subtypes of interest for preclinical drug trials. We exemplified this by evaluating the UAE inhibitor TAK-243 in *BAP1*-deficient ccRCC (Hyer et al., 2018; Wertz and Wang, 2019). PK and PD testing demonstrated plasma concentrations in mice greater than in humans (NCT02045095) and intratumoral UAE inhibition. Despite this, TAK-243 was ineffective. TG lines may also be used to evaluate chemicals or drugs

emerging from screens (Wolff et al., 2015; Chen et al., 2016b; Ingels et al., 2014; Cho et al., 2016; Zhao et al., 2017; Elbanna et al., 2020). As an example, following up on a chemical genetic screen that identified homoharringtonine as synthetic lethal with VHL loss, the drug was repurposed against ccRCC in TGs (Wolff et al., 2015). We identified several TGs with potentially actionable mutations. They included a pRCC line with a *BRAF*V600E mutation (XP156) as well as several TG lines with *BRCA1/BRCA2* mutations (Table S8). Although these mutations are rare in RCC, they may predict responsiveness to drugs already approved by the FDA for other indications (Paluch-Shimon and Cardoso, 2021; Zaman et al., 2019). We also identified a TG line (XP483) with a homozygous *MLH1* mutation that had a high tumor mutational burden, suggesting a mismatch repair defect. The TG and the corresponding parent tumor expressed high levels of PD-L1 consistent with the unique sensitivity of these tumors to PD-1/PD-L1-targeted therapies (Mouw et al., 2017). The TG platform can also be used to identify predictive biomarkers (Chen et al., 2016b). In addition, because TGs appear to be a more suitable source for efficient generation of tumor cell lines (Borodovsky et al., 2017), they can be used to expand the number of RCC cell lines available for *in vitro* drug screens or other studies.

TGs can also be used to dissect mechanisms of drug action. In particular, TGs enable dissecting the effects of drugs on tumor versus stroma and assessing the relative contribution of each to the drug effect. Inasmuch as the system involves two independent components—tumors from affected individuals and host mice—and both are amenable to genetic manipulation, the relative contribution of particular targets in one or another compartment to drug efficacy can be ascertained (unpublished data).

Another potential application is in the study of mechanisms of resistance. As an example, we reported that, by subjecting TG-bearing mice to prolonged therapy with a HIF-2 $\alpha$  inhibitor, acquired resistance developed, resulting in acquisition of a gatekeeper mutation in HIF-2 $\alpha$ , which we later validated in patients (Chen et al., 2016b; Courtney et al., 2020). TGs can also extend studies of acquired resistance by using tumor samples collected after progression in affected individuals. Indeed, our library contains 30 TG lines from metastases of individuals treated previously with a variety of systemic therapies (Table S1).

### Limitations of the study

There are noteworthy limitations to using TGs, however. (1) TG models are established in immunocompromised mice. This limits their utility for evaluating the efficacy of immunotherapy. However, TGs may be suitable for evaluating adoptive T cell transfer *ex vivo* (Kashima et al., 2020), which is an emerging approach (Majzner and Mackall, 2019). (2) Repeated passaging has the potential to result in genomic drift and development of mutations over time (Ben-David et al., 2017). Notably, however, among different tumor types, RCC TGs are among the most stable (Ben-David et al., 2017), and this is consistent with our previous (Peña-Llopis et al., 2012; Sivanand et al., 2012; Wang et al., 2018) and current results. (3) TGs do not capture intratumoral heterogeneity (Turajlic et al., 2018a). However, this also furnishes the opportunity to dissect tumor heterogeneity by characterizing TGs derived from different regions of a tumor.

TG models play an integral role in advancing research in kidney cancer and other tumor types. By sharing our comprehensive RCC TG platform and extensively discussing potential applications, we hope to pave the way for further advances to ultimately benefit affected individuals, who, by gifting their tumors, set the foundation of our UTSW KCP TG platform.

## STAR\*METHODS

### RESOURCE AVAILABILITY

**Lead contact**—Further information and requests for resources and reagents should be directed to and will be fulfilled by the lead contact, James Brugarolas (James.Brugarolas@UTSouthwestern.edu)

**Materials availability**—Cryopreserved tumorgraft tissue can be obtained by submitting a request to (KCP@utsouthwestern.edu).

**Data and code availability**—Tumorgraft sample raw sequencing data files (WES and RNaseq) for patients providing consent (n = 121 samples) (see Table S7) have been deposited to the European Genome-phenome Archive (EGA). Data can be accessed at the following EGA Study ID: EGAS00001005516. All code used to analyze the data is listed in the key resources table and is publicly available. Any additional information required to reanalyze the data reported in this paper is available from the lead contact upon request.

### EXPERIMENTAL MODEL AND SUBJECT DETAILS

**Human subjects**—Patients enrolled in the study provided written consent allowing the use of discarded surgical samples for research purposes including genetic studies according to an Institutional Review Board-approved protocol. Eligible patients were prospectively enrolled between January 1, 2008 and December 31, 2019. A total of 148 patients were included in this study. All clinicopathologic characteristics were collected prospectively in a centralized database, a deidentified version of which is made available in Table S5.

**Animal models**—Typically, 4- to 6-week-old male or female non-obese diabetic/severe combined immunodeficient NOD.CB17-Prkdc<sup>scid</sup> (NOD/SCID) mice (obtained originally from the UTSW Breeding Core) were implanted with tumor samples for TG generation. Animals were housed in laminar flow cages maintained at 22 °C, under a 12-hour light / dark cycle. The mice were permitted free access to tap water and commercialized food, throughout the experiment. Tumorgraft studies were based on our approved protocol by the University of Texas Southwestern Medical Center Institutional Animal Care and Use Committee (IACUC) in compliance with the United States Public Health Service Standards and National Institute of Health guidelines.

### METHOD DETAILS

**Nomenclature and annotation**—Detailed explanations can be found in Table S4. All TG lines are denoted by an “XPID,” which consists of numeric values following “XP.” An “XPID” corresponds to a TG line derived from a particular sample from a patient

(i.e., tumor, thrombus, etc.), and several “XPIDs” may be derived from a single patient. A unique patient ID “PatientID” is assigned corresponding to all the TGs (XPIDs) derived from the same patient, and it is typically the first “XPID” established for the particular patient (this “XPID” generally corresponds to the nephrectomy tumor sample, though there are exceptions). Samples used for genomic sequencing are labeled with a “SampleID” which utilizes the “Root Tree” nomenclature format (see Table S4). This format was designed so that one could easily identify samples from the same patient, the source of the sample, and the TG cohort. Accordingly, the “SampleID” contains information regarding the source of the tumor (N, Normal; T, Tumor; Thp/d, Thrombus Proximal/Distal; M, Metastasis), the tissue type (TG, Tumorgraft), the mouse cohort (i.e., c0, c1, c2).

**Tissue processing and implantation**—Surgical schedules were screened weekly for RCC patients undergoing tumor excisions or biopsies. Inclusion criteria were largely based on imaging and included multiple primaries, recurrent tumors, evidence of local invasion, lymphadenopathy, or distant metastasis. For T1N0M0 and T2N0M0 primary tumors a size threshold of 5 cm was initially used between 2008–2012, 7 cm between 2013–2014, and 10 cm from 2015 onward. We adopted these criteria to select for tumors with higher chances of engraftment (Sivanand et al., 2012). Patients were excluded if they were known to be positive for hepatitis B virus, hepatitis C virus, HIV, or methicillin-resistant *Staphylococcus aureus* (MRSA). Tumors having previously undergone radiation were generally excluded. Luminal metastases in the colon or the airway were also generally excluded from implantation in mice to avoid bacterial contamination.

Tumors were typically processed within 2–3 hours of surgical removal. Processing was conducted under sterile conditions to minimize contamination. Tumors were placed in 1% (vol/vol) penicillin-streptomycin (pen-strep) solution in phosphate-buffered saline, and cut into 8 to 27 mm<sup>3</sup> fragments for: (i) implantation into mice (~15 fragments with a diameter of 2 mm; 2–3 per mouse), (ii) long-term preservation in DMSO (~30 fragments of 2 mm), (iii) histological staining (Formalin Fixation and Paraffin Embedding, FFPE) (3–5 mm fragments), and (iv) flash freezing (FF) for molecular studies (1–2 fragments of 5 mm), as described previously (Pavía-Jiménez et al., 2014) and illustrated in Figure 1.

Tumors were implanted orthotopically under the renal capsule as previously described (Pavía-Jiménez et al., 2014). Tumor growth was typically assessed once weekly by physical examination. When tumors reached ~20 mm in greatest diameter or mice became ill, euthanasia was performed according to IACUC procedures. Alternatively, mice were euthanized at ~140 days following tumor implantation if no tumor growth was appreciable. At the time of mouse death or euthanasia, tumors were routinely explanted and examined histologically by a genitourinary pathologist, and screened for evidence of lymphoproliferative tissue (P.K.). Tumors were passaged serially into subsequent cohorts of NOD/SCID mice orthotopically. Biobanking (as described above) with simultaneous DMSO cryopreservation, as well as FF and FFPE, occurred at the time of tumor passaging (Pavía-Jiménez et al., 2014).

Stable engraftment was defined as histologically confirmed growth in two subsequent cohorts of mice (i.e., tumor growth in c0 and c1). TG lines that demonstrated substantial

growth in c0 but were not implanted into c1 for technical reasons (i.e., infection risk, colony size, etc.) were included if the collected tumor in c0 was > 1cm in diameter. Information regarding each mouse was maintained in a database and updated in real time including: tumorgraft number, cohort, and (at the time of mouse death) tumor size, number of mice passaged, and tissue storage. As NOD/SCID mice develop thymoma as they age (Pavía-Jiménez et al., 2014), presence of thymic enlargement was also recorded.

Relevant clinicopathological information, including demographics, treatment history, and path report details (included in Table S5) was inputted at the time of implantation using the electronic medical record and pathology report. Tumor staging was evaluated according to the American Joint Committee on Cancer staging guidelines at the time of tumor extraction. Survival data used in Figure S3C was obtained using Kidney Cancer Explorer, an Institutional Review Board-approved, i2b2-based queryable database that integrates clinicopathologic data automatically extracted from the electronic medical record sponsored by the UTSW Kidney Cancer Program and the Lyda Hill Department of Bioinformatics Core Facility.

**Tissue processing for genomic studies**—Flash frozen samples preserved at  $-80^{\circ}\text{C}$  were processed while on dry ice. Tumor content was inferred through pathological analyses of flanking sections oriented using pathology dyes (StatLab Medical Products). Samples were selected on the basis of tumor content (> 70% tumor nuclei) and viability (absence of necrosis). Nucleic acid was extracted and purified from fresh frozen tumorgraft tissue as previously described (Peña-Llopis and Brugarolas, 2013). Briefly, DNA and RNA were simultaneously extracted and purified using AllPrep DNA/RNA Mini Kit (QIAGEN, 80204). Nucleic acid yield and quality were assessed using a NanoDrop ND-1000 spectrophotometer. RNA quality was further evaluated by quantifying the abundance of ribosomal RNA fractions with Experion (Bio-Rad) and/or Agilent 2100 Bioanalyzer.

**Whole exome sequencing (WES)**—Extracted DNA from tumorgraft tissue with adequate quality was submitted to Genentech (n = 122 samples) or the New York Genome Center (n = 3 samples) for WES. Sequencing was conducted using the HiSeq2500 platform (Illumina) to generate  $2 \times 75$ -bp paired-end data (Durinck et al., 2015). In order to remove contaminating mouse reads from tumorgraft Exome-seq libraries, reads were aligned to a concatenated reference by merging human reference (GRCh38) and mouse reference (GRCh38m) genomes by BWA-MEM (Li and Durbin, 2009; Jo et al., 2019). Reads aligned to mm10 were removed (Jo et al., 2019), and remaining reads underwent subsequent processing by Samtools (Danecek et al., 2021) and Picard (<https://broadinstitute.github.io/picard>) to ensure proper file formatting and to mark duplicates. Alignments were then recalibrated and realigned using GATK (DePristo et al., 2011; McKenna et al., 2010; Van der Auwera et al., 2013). A median coverage post-mouse read filtration of  $\sim 85\text{X}$  and  $\sim 105\text{X}$  was achieved for exome libraries of tumorgraft and normal samples respectively. To detect somatic variants, we used MuTect2 (Cibulskis et al., 2013), FreeBayes (Garrison and Marth, 2012), and Strelka2 (Kim et al., 2018). To further remove contaminating mouse alleles, we filtered out recurrent human aligning mouse alleles (HAMA) (Jo et al., 2019). To filter false positive calls in tumorgraft samples, we employed the following filtering

method: variants were removed if any of the following criteria were met: (1) there were less than 8 supporting alternative reads; (2) there were less than 10 total reads; (3) minor allele frequency was less than 0.15; or (4) variant was predicted by only a single variant calling tool. VCF2MAF (<https://github.com/mskcc/vcf2maf>) was used to annotate SNVs, indels, and protein sequence changes. Finally, in order to identify possible disease-causing variants in Table S8, we removed variants in noncoding regions and those in known repeat regions. A MAF cutoff of 0.05 was used in Figure S1B for a comparison of MAF between paired TGs and parent tumors. Oncoprints in Figure 3 were generated using the R package “ComplexHeatmap” (Gu et al., 2016). Samples originating from the same patient with discrepant mutation calling in driver genes were manually reviewed using the integrated genome viewer (IGV) (<https://software.broadinstitute.org/software/igv/>). Mutations detected in IGV but filtered (typically due to low sequencing depth) were included in the figure and annotated as such, but are not annotated in Table S8. “Multihit” mutations were defined as non-adjacent or overlapping indels or SNVs occurring within a single gene per sample.

**RNA sequencing**—The libraries were multiplexed three per lane and sequenced on a HiSeq2500 platform to obtain, on average, ~150 million paired-end ( $2 \times 75$ -bp) reads per sample (Durinck et al., 2015). In order to remove contaminating mouse reads from tumorgrafts, reads were aligned to a concatenated reference by merging human reference (GRCh38) and mouse reference (GRCh38m) genomes by hisat2 (Kim et al., 2019). Reads aligned to the mouse genome were removed (Jo et al., 2019). Abundance of genes was determined using FeatureCounts (Liao et al., 2014) and GENOCODE 33 (Frankish et al., 2019). Transcripts per million (TPM) values were calculated from gene read counts. TPM values were then  $\log_2$  transformed.

**Gene expression analyses**—TPM values from TG samples and matching primaries and normal samples were pooled. Genes with a TPM value of 0 in 80% or more of samples were removed ( $n = 17,534$  resulting in 39,600). The top 25% most variable genes (by coefficient of variation) were selected ( $n = 9,900$ ), and principal component analysis (PCA) was performed. In order to directly compare tumor and tumorgraft samples, overlapping eTME genes (Wang et al., 2018) ( $n = 430$ ) were removed, and PCA was performed on the expression data of the remaining 9,470 genes. Hierarchical clustering was performed in this gene space using Pearson Correlation and Ward’s linkage and the resulting dendrogram was visualized. All analyses were done in R v4.03.

Count data for TCGA tumor samples utilized in generation of the KIPAN gene signature (Chen et al., 2016a) were accessed through the Genomic Data Commons Data Portal [<https://portal.gdc.cancer.gov>]. TPM values were calculated from counts, and expression data from TCGA samples and UTSW TG and corresponding patient tumor samples were pooled on the basis of the 800 genes comprising the KIPAN gene signature (Chen et al., 2016a). Values were then  $\log_2$  transformed and subjected to batch effect removal (i.e., TCGA versus UTSW) via the “ComBat” function of the “SVA” R package (Leek et al., 2012). Sample histology (ccRCC, pRCC, chRCC) was used as the covariate in the model matrix. In order to compare the tumor specific transcriptome, overlapping eTME (Wang et al., 2018) genes ( $n = 124$ ) were removed, and the resulting 676 genes were used in

downstream analysis. Uniform Manifold Approximation and Projection (Package “umap”; <https://cran.r-project.org/web/packages/umap>) algorithm was then used to transform the data to a 2-dimension map for visualization and analysis. We used the default parameters for UMAP with the exception of “n\_neighbors” which was set to 50 to reduce spurious clustering. For visualization purposes, TCGA chRCC samples (n = 77/896) were filtered out from Figure 4 and Data S1. An interactive plot (Data S1) was generated using the “plotly” package (<https://plotly.com/r/>). UTSW samples were assigned a predicted “KIPAN cluster” on the basis of the most frequent cluster within a perimeter of n = 15 neighbors. For samples where there was a tie for the most frequent neighbor (i.e., equal numbers of the top two clusters among the 15 nearest neighbor) the sample was coded as indeterminate (Figures S3 and 5). For survival analysis, a patient was assigned the most aggressive cluster identified in the corresponding samples. All analyses were done in R v4.03.

**Metabolomics**—Metabolomic analyses were conducted in multiple TGs and normal kidney tissues from 16 individual orthotopically-implanted lines. 1–3 biological replicates were obtained from each TG line, and each biological replicate was further divided into 3 technical replicates for a total of 134 samples. Samples were snap-frozen in liquid nitrogen within 3 minutes of sacrificing the animal to minimize metabolite alterations. Subsequently, they were weighted (~30mg) and homogenized in 80% methanol in water. Supernatants were dried overnight and reconstituted in 100  $\mu$ L of 0.03% formic acid. Reconstituted samples were analyzed in AB QTRAP 5500 liquid chromatography/triple quadrupole mass spectrometer (Applied Biosystems SCIEX, Foster City, CA) (Chong et al., 2019). Peak integration was performed using the MultiQuant software version 2.1. The relative abundance of each metabolite was calculated by normalizing the area under the curve for all metabolites to total ion count (TIC) in each sample as previously described (Mullen et al., 2014). Raw data were further analyzed using Metaboanalyst 4.0 (Chong et al., 2019). Log<sub>2</sub> median normalized TIC values were used for Partial least-squares - discriminant analysis (PLS-DA) using R v4.03 (A.K.).

**Immunohistochemistry (IHC)**—IHC was performed on TGs using Dako Autostainer Link 48 as previously described (Sivanand et al., 2012). Primary antibodies were obtained from BioCare (PD-L1, 1:300 dilution, ACI 3171A). Standardized positive and negative controls were utilized for PD-L1 immunostaining.

**Synthesis of radiolabeled atezolizumab**—The humanized monoclonal antibody (mAb) Atezolizumab (ATZ; Tecentriq®, 60 mg/mL) was obtained from the UTSW pharmacy. In house synthesis of zirconium radiolabeled ATZ (<sup>89</sup>Zr-ATZ) was performed as previously described (Vosjan et al., 2010). Briefly, the ATZ buffer solution was replaced with 1X PBS (Sigma Aldrich) using Amicon 50 kDa centrifuge columns (EMD Millipore). This solution was diluted with 0.1 M sodium carbonate (pH ~9) and conjugated with the chelator p-SCN-Bn-Deferoxamine (DFO) dissolved in anhydrous dimethyl sulfoxide by gentle mixing at 300 rpm for 45 min at room temperature. The resultant DFO-ATZ conjugate was purified using Amicon 50 kDa columns and stored in 0.2 M HEPES pH ~7 at -80°C until use. The radionuclide <sup>89</sup>Zr was produced at the UTSW Cyclotron Research Program by a <sup>89</sup>Y(p,n)<sup>89</sup>Zr reaction upon cyclotron bombardment of a yttrium foil solid

target (Alfa Aesar), followed by separation, purification and elution of  $^{89}\text{Zr}$  in 1 M oxalic acid. The DFO-ATZ was subsequently radiolabeled with  $^{89}\text{Zr}$  by first neutralizing the  $^{89}\text{Zr}$ -oxalate to pH ~7 using 2 M sodium carbonate and 5 M sulfuric acid, then mixing with DFO-ATZ solution at specific activity of ~5 mCi/mg DFO-ATZ and incubating for 40 min on a shaker (at 300 rpm at 21°C). This resulted in crude  $^{89}\text{Zr}$ -ATZ, which was purified by Zeba® (Pierce Biotechnology) spin columns and eluted in 0.2 M sodium acetate with 5 mg/mL gentisic acid (pH 5.5). Purified  $^{89}\text{Zr}$ -ATZ was subjected to quality control analyses prior to release for use.

**Mouse  $^{89}\text{Zr}$ -ATZ PET studies**—TGs were selected on the basis of PD-L1 expression by immunohistochemistry (IHC). Mouse PET imaging was performed using Siemens Inveon PET/CT Multi-Modality system with an effective spatial resolution of 1.4 mm at the center of field of view (FOV). The mice received 100  $\mu\text{Ci}$  of  $^{89}\text{Zr}$ -ATZ intravenously via tail vein injection. PET imaging was performed ~7 days post injection while mice were sedated with 1.5% isoflurane. PET images were reconstructed into a single frame using the 3D Ordered Subsets Expectation Maximization (OSEM3D/MAP) algorithm.

**Human  $^{89}\text{Zr}$ -ATZ PET/CT**—Images were acquired on a Siemens Biograph mCT scanner from participants in the clinical trial “ $^{89}\text{Zr}$ -DFO-Atezolizumab Immuno-PET/CT in Patients with Locally Advanced or Metastatic Renal Cell Carcinoma” (NCT04006522; PI, Brugarolas). Subjects were scanned from the skull base to mid-thigh, 6–7 days post-injection. Emission scans were obtained in 3-D mode for 7 minutes per position. CT was performed for attenuation correction and anatomic localization. A low dose CT scan was acquired using the manufacturer’s CARE DOSE4D protocol. Images were reconstructed with a 500mm field of view into a  $128 \times 128$  matrix using iterative ordered-subset expectation maximization (8 iterations; 12 subsets).

**Pharmacokinetic studies of TAK-243 in NOD/SCID mice**—6-week-old NOD/SCID mice bearing subcutaneous TGs were used for pharmacokinetic (PK) analysis. They were administered a single IV dose of 25 mg/kg of TAK-243 formulated in 20% DMSO and 80% 2-Hydroxy- $\beta$ -cyclodextrin (0.1 ml/mouse). Whole blood, kidney, and tumor samples were collected at 15 min, 24 hr, 48 hr and 72 hr into acidified citrate dextrose (ACD) treated tubes. Plasma was processed from whole blood by centrifugation for 10 min at 9,600x g. All tissues (kidney and tumor) were washed with PBS, then weighed and snap frozen in liquid nitrogen. Tissues were homogenized in 3x volume of PBS by weight. Aliquots of plasma or tissue homogenates were cleared of protein by mixing with a two-fold volume of methanol containing 0.15% formic acid and 18.75 ng/ml n-benzylbenzamide internal standard (IS) followed by vortexing and centrifugation to pellet precipitated protein. TAK-243 levels in the resulting supernatant were measured by LC/MS using a Sciex 4000QTRAP coupled to a Shimadzu LC. Standards, prepared by spiking blank plasma or tissue homogenates from un-injected mice with varying concentrations of TAK-243, were processed following the same procedure. Chromatography conditions were as follows. Buffer A consisted of water + 0.1% formic acid and Buffer B consisted of methanol + 0.1% formic acid. The column flow rate was 1.5 ml/min using an Agilent C18 XDB, 5 micron packing 50 X 4.6 mm size column. The gradient conditions were: 0.01 – 1.0 min, 3% B; 1.0 – 1.5 min, increase to

100% B; 1.5 – 3.0, hold 100% B; 3.0 – 3.1 min, gradient decrease 3% B, 3.1 – 4.0 hold 3% B. TAK-243 was detected in MRM mode by following the precursor to fragment ion transition 520.033 to 242.00. N-benzylbenzamide (transition 212.1 to 91.1) was used as an internal standard. A value 3-fold above the signal obtained from blank whole blood was designated as the limit of detection (LOD). The limit of quantitation (LOQ) was defined as the lowest concentration at which back calculation yielded a concentration within 20% of theoretical and which was above the LOD. The LOQ for TAK-243 was 1 ng/ml for tissues and 0.5 ng/ml for plasma. In general, back calculation of points yielded values within 15% of theoretical over five orders of magnitude (1 ng/ml to 10,000 ng/ml). Pharmacokinetic parameters were calculated in sparse sampling mode using the noncompartmental analysis tool of WinNonlin (Pharsight Corporation).

**Pharmacodynamic studies by western blot**—Western blot was conducted on tumor derived from vehicle and TAK-243 treated groups using previously described protocols (Peña-Llopis et al., 2012). Briefly, excised tumor was mechanically dissociated then washed with PBS and lysed in lysis buffer [50 mM Tris-HCl (pH 7.4), 250 mM NaCl, 0.5% Igepal] supplemented with protease inhibitors [0.1 μM aprotinin (USB), 0.02 mM leupeptin (USB), 0.01 mM pepstatin (USB), 0.5 mM benzamidine (Sigma), 0.5 mM PMSF (Sigma), 0.01 M NaF (Sigma)] and phosphatase inhibitors [2 mM imidazole (Sigma), 1.15 mM sodium molybdate (Sigma), 1 mM sodium orthovanadate (Sigma), 5 nM microcystin (Calbiochem)] for 10 minutes at 4°C. Lysates were cleared by centrifugation at 16000 g for 10 minutes, and protein concentration was measured by Bradford's method (BioRad). Protein lysates were supplemented with 3x SDS-loading buffer (6.7% SDS, 33.3% glycerol, 300 mM DTT, bromophenol blue) and denatured by boiling for 10 minutes. Similar amounts of protein were resolved by SDS-PAGE, transferred to a nitrocellulose membrane (BioRad), blocked with 5% milk in TBST (10 mM Tris-HCl, 15 mM NaCl, 0.1% Tween-20) and probed for the desired primary antibodies followed by appropriate secondary antibodies conjugated to HRP and the signal was detected by chemiluminescence [mixing 1:1 solution 1 (2.5 mM luminol, 0.4 mM pCoumaric acid, 0.1 M Tris-HCl) and solution 2 (0.015% H<sub>2</sub>O<sub>2</sub>, 0.1 M Tris-HCl)]. Primary antibodies were purchased at Cell Signaling: ubiquityl-Histone H2A (Lys119) antibody (Cat ID: 26498, 1:1000 dilution) and ubiquityl-Histone H2B antibody (Lys120) (Cat ID: 5546, 1:1000 dilution)

**Drug trials**—Tumor fragments from stable TG lines were implanted subcutaneously in ~4–6 week-old NOD/SCID mice. When tumor volumes reached ~300 mm<sup>3</sup>, mice were allocated into different treatment groups as previously described (Sivanand et al., 2012; Pavía-Jiménez et al., 2014). TAK-243 (MLN7243) (Chemietek) was administered IV every 72 hours at 25 mg/kg in 20% 2-hydroxypropyl-β-cyclodextrin (HPβCD). Rapamycin (positive control) was administered intraperitoneally at 0.5 mg/kg in 5% ethanol, 5% PEG400, 5% Tween 80, and 85% D5W every 48 hours. Mouse weight and tumor volumes were typically assessed three times per week. Tumor volume was measured using calipers and calculated as previously reported (Pavía-Jiménez et al., 2014). Data are reported as tumor means ± SD.

## QUANTIFICATION AND STATISTICAL ANALYSIS

Baseline clinicopathologic characteristics were summarized for patients from whom TG models were successfully generated using descriptive statistics. For most WES and RNAseq analysis, results were descriptive. WES analyses: Comparative analysis of tumor mutational burden and median allele frequency was performed using paired Wilcoxon signed rank test (Figures S2B and S2C). Analysis of tumor mutational burden and cohort was performed using linear mixed modeling controlling for inter-TG line variability (Figure S2D). Metabolomics: The most variable metabolites among groups were selected by analysis of variance (ANOVA) comparing the three groups utilizing a Benjamini-Hochberg adjusted p value of 0.05. Statistical significance of differences in relative metabolite concentrations among groups was calculated using a mixed model with a compound symmetric covariance structure of the log<sub>2</sub> transformed metabolites shown in the pathway map (Figure 5B). All statistical analyses were performed in R v4.03 by a dedicated biostatistician (A.C.).

## Supplementary Material

Refer to Web version on PubMed Central for supplementary material.

## ACKNOWLEDGMENTS

More than 900 individuals at UTSW and its affiliated county hospital donated their samples. We acknowledge the support and cooperation from Parkland Health and Hospital System staff for voluntarily participating in study data collection. The TG resource was supported by an American Cancer Society Research Scholar grant (115739) and National Institutes of Health grant P50CA196516. Genomic studies were funded primarily by S.S. from Genentech/Roche. Metabolomic studies were funded through an NCI Outstanding Investigator Award (R35CA22044901 to R.J.D.). We acknowledge the UTSW Tissue Resource and Small Animal Imaging Resource, which are supported in part by P30CA142543; the Cyclotron and Radiochemistry Program, supported in part by the Cancer Prevention and Research Institute of Texas (CPRIT; RP170638 and RP110771), and the institutionally supported Preclinical Pharmacology Core. R.E. is supported by the Burroughs Wellcome Fund, O.R.T. by the FSEOM/Fundación Cris Contra el Cancer 2018, O.K.O. by the Robert W. Parkey, M.D. Distinguished Professorship in Radiology, I.P. by R01CA154475, N.S. by Ruth L. Kirschstein National Research Service Award T32 CA136515-09 and the Physician Scientist Training Program, B.L.C. by funds from CPRIT (RP150596), P.K. through an endowment from the Jan and Bob Pickens Distinguished Professorship in Medical Science and Brock Fund for Medical Science Chair in Pathology, and J.B. by the Sherry Wigley Crow Cancer Research Endowment in Honor of Robert Lewis Kirby, MD.

### DECLARATION OF INTERESTS

J.B. is an employee/paid consultant for Arrowhead, Calithera, Esai, Exelixis, and Johnson & Johnson and reports receiving commercial research grants from Arrowhead. J.B. and X.S. have a patent application on [<sup>18</sup>F]PT2385. I.P. reports personal fees from Bayer Healthcare and Health Tech International, personal fees for serving in an Advisory Committee for Merck, and others from Philips Healthcare, all outside of the submitted work. R.J.D. is a founder of Atavistik Bio and a member of the Scientific Advisory Boards of Agios Pharmaceuticals, Vida Ventures, and Nirogy Therapeutics.

## REFERENCES

- Bakouny Z, Braun DA, Shukla SA, Pan W, Gao X, Hou Y, Flaifel A, Tang S, Bosma-Moody A, He MX, et al. (2021). Integrative molecular characterization of sarcomatoid and rhabdoid renal cell carcinoma. *Nat. Commun.* 12, 808. [PubMed: 33547292]
- Ben-David U, Ha G, Tseng Y-Y, Greenwald NF, Oh C, Shih J, McFarland JM, Wong B, Boehm JS, Beroukhi R, and Golub TR (2017). Patient-derived xenografts undergo mouse-specific tumor evolution. *Nat. Genet.* 49, 1567–1575. [PubMed: 28991255]

- Bi M, Zhao S, Said JW, Merino MJ, Adeniran AJ, Xie Z, Nawaf CB, Choi J, Belldegrün AS, Pantuck AJ, et al. (2016). Genomic characterization of sarcomatoid transformation in clear cell renal cell carcinoma. *Proc. Natl. Acad. Sci. USA* 113, 2170–2175. [PubMed: 26864202]
- Borodovsky A, McQuiston TJ, Stetson D, Ahmed A, Whitston D, Zhang J, Grondine M, Lawson D, Challberg SS, Zinda M, et al. (2017). Generation of stable PDX derived cell lines using conditional reprogramming. *Mol. Cancer* 16, 177. [PubMed: 29212548]
- Brannon AR, Reddy A, Seiler M, Arreola A, Moore DT, Pruthi RS, Wallen EM, Nielsen ME, Liu H, Nathanson KL, et al. (2010). Molecular Stratification of Clear Cell Renal Cell Carcinoma by Consensus Clustering Reveals Distinct Subtypes and Survival Patterns. *Genes Cancer* 1, 152–163. [PubMed: 20871783]
- Brugarolas J, Lotan Y, Watumull L, and Kabbani W (2008). Sirolimus in metastatic renal cell carcinoma. *J. Clin. Oncol.* 26, 3457–3460. [PubMed: 18612163]
- Bukowski RM, Kabbinavar FF, Figlin RA, Flaherty K, Srinivas S, Vaishampayan U, Drabkin HA, Dutcher J, Ryba S, Xia Q, et al. (2007). Randomized phase II study of erlotinib combined with bevacizumab compared with bevacizumab alone in metastatic renal cell cancer. *J. Clin. Oncol.* 25, 4536–4541. [PubMed: 17876014]
- Cai Q, Christie A, Rajaram S, Zhou Q, Araj E, Chintalapati S, Cadeddu J, Margulis V, Pedrosa I, Rakheja D, et al. (2020). Ontological analyses reveal clinically-significant clear cell renal cell carcinoma subtypes with convergent evolutionary trajectories into an aggressive type. *EBioMedicine* 51, 102526. [PubMed: 31859241]
- Cancer Genome Atlas Research Network; Linehan WM, Spellman PT, Ricketts CJ, Creighton CJ, Fei SS, Davis C, Wheeler DA, Murray BA, Schmidt L, et al. (2016). Comprehensive Molecular Characterization of Papillary Renal-Cell Carcinoma. *N. Engl. J. Med.* 374, 135–145. [PubMed: 26536169]
- Cancer Genome Atlas Research Network (2013). Comprehensive molecular characterization of clear cell renal cell carcinoma. *Nature* 499, 43–49. [PubMed: 23792563]
- Chen F, Zhang Y, enbabao lu Y, Ciriello G, Yang L, Reznik E, Shuch B, Micevic G, De Velasco G, Shinbrot E, et al. (2016a). Multilevel Genomics-Based Taxonomy of Renal Cell Carcinoma. *Cell Rep.* 14, 2476–2489. [PubMed: 26947078]
- Chen W, Hill H, Christie A, Kim MS, Holloman E, Pavia-Jimenez A, Homayoun F, Ma Y, Patel N, Yell P, et al. (2016b). Targeting renal cell carcinoma with a HIF-2 antagonist. *Nature* 539, 112–117. [PubMed: 27595394]
- Chen Y-B, Xu J, Skanderup AJ, Dong Y, Brannon AR, Wang L, Won HH, Wang PI, Nanjangud GJ, Jungbluth AA, et al. (2016c). Molecular analysis of aggressive renal cell carcinoma with unclassified histology reveals distinct subsets. *Nat. Commun.* 7, 13131. [PubMed: 27713405]
- Cho H, Du X, Rizzi JP, Liberzon E, Chakraborty AA, Gao W, Carvo I, Signoretti S, Bruick RK, Josey JA, et al. (2016). On-target efficacy of a HIF-2 $\alpha$  antagonist in preclinical kidney cancer models. *Nature* 539, 107–111. [PubMed: 27595393]
- Chong J, Wishart DS, and Xia J (2019). Using MetaboAnalyst 4.0 for Comprehensive and Integrative Metabolomics Data Analysis. *Curr. Protoc. Bioinformatics* 68, e86. [PubMed: 31756036]
- Choueiri TK, Motzer RJ, Rini BI, Haanen J, Campbell MT, Venugopal B, Kollmannsberger C, Gravis-Mescam G, Uemura M, Lee JL, et al. (2020). Updated efficacy results from the JAVELIN Renal 101 trial: first-line avelumab plus axitinib versus sunitinib in patients with advanced renal cell carcinoma. *Ann. Oncol.* 31, 1030–1039. [PubMed: 32339648]
- Choueiri TK, Powles T, Burotto M, Escudier B, Bourlon MT, Zurawski B, Oyervides Juárez VM, Hsieh JJ, Basso U, Shah AY, et al. ; Check Mate 9ER Investigators (2021). Nivolumab plus Cabozantinib versus Sunitinib for Advanced Renal-Cell Carcinoma. *N. Engl. J. Med.* 384, 829–841. [PubMed: 33657295]
- Cibulskis K, Lawrence MS, Carter SL, Sivachenko A, Jaffe D, Sougnez C, Gabriel S, Meyerson M, Lander ES, and Getz G (2013). Sensitive detection of somatic point mutations in impure and heterogeneous cancer samples. *Nat. Biotechnol.* 31, 213–219. [PubMed: 23396013]
- Clark DJ, Dhanasekaran SM, Petralia F, Pan J, Song X, Hu Y, da Veiga Leprevost F, Reva B, Lih TM, Chang H-Y, et al. ; Clinical Proteomic Tumor Analysis Consortium (2019). Integrated

- Proteogenomic Characterization of Clear Cell Renal Cell Carcinoma. *Cell* 179, 964–983.e31. [PubMed: 31675502]
- Courtney KD, Bezwada D, Mashimo T, Pichumani K, Vemireddy V, Funk AM, Wimberly J, McNeil SS, Kapur P, Lotan Y, et al. (2018a). Isotope Tracing of Human Clear Cell Renal Cell Carcinomas Demonstrates Suppressed Glucose Oxidation In Vivo. *Cell Metab.* 28, 793–800.e2. [PubMed: 30146487]
- Courtney KD, Infante JR, Lam ET, Figlin RA, Rini BI, Brugarolas J, Zojwalla NJ, Lowe AM, Wang K, Wallace EM, et al. (2018b). Phase I Dose-Escalation Trial of PT2385, a First-in-Class Hypoxia-Inducible Factor-2 $\alpha$  Antagonist in Patients With Previously Treated Advanced Clear Cell Renal Cell Carcinoma. *J. Clin. Oncol.* 36, 867–874. [PubMed: 29257710]
- Courtney KD, Ma Y, Diaz de Leon A, Christie A, Xie Z, Woolford L, Singla N, Joyce A, Hill H, Madhuranthakam AJ, et al. (2020). HIF-2 Complex Dissociation, Target Inhibition, and Acquired Resistance with PT2385, a First-in-Class HIF-2 Inhibitor, in Patients with Clear Cell Renal Cell Carcinoma. *Clin. Cancer Res.* 26, 793–803. [PubMed: 31727677]
- Danecek P, Bonfield JK, Liddle J, Marshall J, Ohan V, Pollard MO, Whitwham A, Keane T, McCarthy SA, Davies RM, and Li H (2021). Twelve years of SAMtools and BCFtools. *Gigascience* 10, giab008. [PubMed: 33590861]
- Davis AA, and Patel VG (2019). The role of PD-L1 expression as a predictive biomarker: an analysis of all US Food and Drug Administration (FDA) approvals of immune checkpoint inhibitors. *J. Immunother. Cancer* 7, 278. [PubMed: 31655605]
- Davis CF, Ricketts CJ, Wang M, Yang L, Cherniack AD, Shen H, Buhay C, Kang H, Kim SC, Fahey CC, et al. ; The Cancer Genome Atlas Research Network (2014). The somatic genomic landscape of chromophobe renal cell carcinoma. *Cancer Cell* 26, 319–330. [PubMed: 25155756]
- de Cubas AA, and Rathmell WK (2018). Epigenetic modifiers: activities in renal cell carcinoma. *Nat. Rev. Urol.* 15, 599–614. [PubMed: 30030490]
- DePristo MA, Banks E, Poplin R, Garimella KV, Maguire JR, Hartl C, Philippakis AA, del Angel G, Rivas MA, Hanna M, et al. (2011). A framework for variation discovery and genotyping using next-generation DNA sequencing data. *Nat. Genet.* 43, 491–498. [PubMed: 21478889]
- DiNatale RG, Sanchez A, Hakimi AA, and Reznik E (2020). Metabolomics informs common patterns of molecular dysfunction across histologies of renal cell carcinoma. *Urol. Oncol.* 38, 755–762. [PubMed: 31155438]
- Durinck S, Stawiski EW, Paviá-Jimeénez é, Modrusan Z, Kapur P, Jaiswal BS, Zhang N, Toffessi-Tcheuyap V, Nguyen TT, Pahuja KB, et al. (2015). Spectrum of diverse genomic alterations define non-clear cell renal carcinoma subtypes. *Nat. Genet.* 47, 13–21. [PubMed: 25401301]
- Elbanna M, Orillion AR, Damayanti NP, Adelaiye-Ogala R, Shen L, Miles KM, Chintala S, Ciamporcerio E, Ramakrishnan S, Ku SY, et al. (2020). Dual inhibition of angiopoietin-TIE2 and MET alters the tumor microenvironment and prolongs survival in a metastatic model of renal cell carcinoma. *Mol. Cancer Ther.* 19, 147–156. [PubMed: 31582532]
- Foglizzo M, Middleton AJ, Burgess AE, Crowther JM, Dobson RCJ, Murphy JM, Day CL, and Mace PD (2018). A bidentate Polycomb Repressive-Deubiquitinase complex is required for efficient activity on nucleosomes. *Nat. Commun.* 9, 3932. [PubMed: 30258054]
- Forbes SA, Beare D, Boutselakis H, Bamford S, Bindal N, Tate J, Cole CG, Ward S, Dawson E, Ponting L, et al. (2017). COSMIC: somatic cancer genetics at high-resolution. *Nucleic Acids Res.* 45 (D1), D777–D783. [PubMed: 27899578]
- Frankish A, Diekhans M, Ferreira AM, Johnson R, Jungreis I, Loveland J, Mudge JM, Sisu C, Wright J, Armstrong J, et al. (2019). GENCODE reference annotation for the human and mouse genomes. *Nucleic Acids Res.* 47 (D1), D766–D773. [PubMed: 30357393]
- Garrison E, and Marth G (2012). Haplotype-based variant detection from short-read sequencing. *arXiv*, arXiv:1207.3907. <https://arxiv.org/abs/1207.3907>.
- Gerlinger M, Rowan AJ, Horswell S, Math M, Larkin J, Endesfelder D, Gronroos E, Martinez P, Matthews N, Stewart A, et al. (2012). Intratumor heterogeneity and branched evolution revealed by multiregion sequencing. *N. Engl. J. Med.* 366, 883–892. [PubMed: 22397650]

- Gerlinger M, Horswell S, Larkin J, Rowan AJ, Salm MP, Varela I, Fisher R, McGranahan N, Matthews N, Santos CR, et al. (2014). Genomic architecture and evolution of clear cell renal cell carcinomas defined by multiregion sequencing. *Nat. Genet.* 46, 225–233. [PubMed: 24487277]
- Grisanzio C, Seeley A, Chang M, Collins M, Di Napoli A, Cheng SC, Percy A, Beroukhi R, and Signoretti S (2011). Orthotopic xenografts of RCC retain histological, immunophenotypic and genetic features of tumours in patients. *J. Pathol.* 225, 212–221. [PubMed: 21710693]
- Gu Z, Eils R, and Schlesner M (2016). Complex heatmaps reveal patterns and correlations in multidimensional genomic data. *Bioinformatics* 32, 2847–2849. [PubMed: 27207943]
- Hahn SA, Seymour AB, Hoque AT, Schutte M, da Costa LT, Redston MS, Caldas C, Weinstein CL, Fischer A, Yeo CJ, et al. (1995). Allelotype of pancreatic adenocarcinoma using xenograft enrichment. *Cancer Res.* 55, 4670–4675. [PubMed: 7553647]
- Hakimi AA, Reznik E, Lee C-H, Creighton CJ, Brannon AR, Luna A, Aksoy BA, Liu EM, Shen R, Lee W, et al. (2016). An Integrated Metabolic Atlas of Clear Cell Renal Cell Carcinoma. *Cancer Cell* 29, 104–116. [PubMed: 26766592]
- Heng DY, Xie W, Regan MM, Warren MA, Golshayan AR, Sahi C, Eigel BJ, Ruether JD, Cheng T, North S, et al. (2009). Prognostic factors for overall survival in patients with metastatic renal cell carcinoma treated with vascular endothelial growth factor-targeted agents: results from a large, multicenter study. *J. Clin. Oncol.* 27, 5794–5799. [PubMed: 19826129]
- Hudes G, Carducci M, Tomczak P, Dutcher J, Figlin R, Kapoor A, Staroslawska E, Sosman J, McDermott D, Bodrogi I, et al. ; Global ARCC Trial (2007). Temsirolimus, interferon alfa, or both for advanced renal-cell carcinoma. *N. Engl. J. Med.* 356, 2271–2281. [PubMed: 17538086]
- Hyer ML, Milhollen MA, Ciavarrri J, Fleming P, Traore T, Sappal D, Huck J, Shi J, Gavin J, Brownell J, et al. (2018). A small-molecule inhibitor of the ubiquitin activating enzyme for cancer treatment. *Nat. Med.* 24, 186–193. [PubMed: 29334375]
- Ingels A, Zhao H, Thong AE, Saar M, Valta MP, Nolley R, Santos J, and Peehl DM (2014). Preclinical trial of a new dual mTOR inhibitor, MLN0128, using renal cell carcinoma tumorgrafts. *Int. J. Cancer* 134, 2322–2329. [PubMed: 24243565]
- Jang C, Chen L, and Rabinowitz JD (2018). Metabolomics and isotope tracing. *Cell* 173, 822–837. [PubMed: 29727671]
- Jin J, Li X, Gygi SP, and Harper JW (2007). Dual E1 activation systems for ubiquitin differentially regulate E2 enzyme charging. *Nature* 447, 1135–1138. [PubMed: 17597759]
- Jo S-Y, Kim E, and Kim S (2019). Impact of mouse contamination in genomic profiling of patient-derived models and best practice for robust analysis. *Genome Biol.* 20, 231. [PubMed: 31707992]
- Jonasch E, Plimack ER, Bauer T, Merchan JR, Papadopoulos KP, McDermott DF, Michaelson MD, Appleman LJ, Thamake S, Zojwalla N, and Choueiri TK (2019). 911PDA first-in-human phase I/II trial of the oral HIF-2 $\alpha$  inhibitor PT2977 in patients with advanced RCC. *Ann. Oncol.* 30.
- Joseph RW, Kapur P, Serie DJ, Eckel-Passow JE, Parasramka M, Ho T, Cheville JC, Frenkel E, Rakheja D, Brugarolas J, and Parker A (2014). Loss of BAP1 protein expression is an independent marker of poor prognosis in patients with low-risk clear cell renal cell carcinoma. *Cancer* 120, 1059–1067. [PubMed: 24382589]
- Kapur P, Peña-Llopis S, Christie A, Zhrebker L, Pavía-Jiménez A, Rathmell WK, Xie X-J, and Brugarolas J (2013). Effects on survival of BAP1 and PBRM1 mutations in sporadic clear-cell renal-cell carcinoma: a retrospective analysis with independent validation. *Lancet Oncol.* 14, 159–167. [PubMed: 23333114]
- Kapur P, Christie A, Raman JD, Then MT, Nuhn P, Buchner A, Bastian P, Seitz C, Shariat SF, Bensalah K, et al. (2014). BAP1 immunohistochemistry predicts outcomes in a multi-institutional cohort with clear cell renal cell carcinoma. *J. Urol.* 191, 603–610. [PubMed: 24076305]
- Karam JA, Zhang XY, Tamboli P, Margulis V, Wang H, Abel EJ, Culp SH, and Wood CG (2011). Development and characterization of clinically relevant tumor models from patients with renal cell carcinoma. *Eur. Urol.* 59, 619–628. [PubMed: 21167632]
- Kashima S, Maeda T, Masuda K, Nagano S, Inoue T, Takeda M, Kono Y, Kobayashi T, Saito S, Higuchi T, et al. (2020). Cytotoxic T Lymphocytes Regenerated from iPS Cells Have Therapeutic Efficacy in a Patient-Derived Xenograft Solid Tumor Model. *iScience* 23, 100998. [PubMed: 32259478]

- Kawai T, and Akira S (2010). The role of pattern-recognition receptors in innate immunity: update on Toll-like receptors. *Nat. Immunol.* 11, 373–384. [PubMed: 20404851]
- Kim S, Scheffler K, Halpern AL, Bekritsky MA, Noh E, Källberg M, Chen X, Kim Y, Beyter D, Krusche P, and Saunders CT (2018). Strelka2: fast and accurate calling of germline and somatic variants. *Nat. Methods* 15, 591–594. [PubMed: 30013048]
- Kim D, Paggi JM, Park C, Bennett C, and Salzberg SL (2019). Graph-based genome alignment and genotyping with HISAT2 and HISAT-genotype. *Nat. Biotechnol.* 37, 907–915. [PubMed: 31375807]
- Leek JT, Johnson WE, Parker HS, Jaffe AE, and Storey JD (2012). The sva package for removing batch effects and other unwanted variation in high-throughput experiments. *Bioinformatics* 28, 882–883. [PubMed: 22257669]
- Li H, and Durbin R (2009). Fast and accurate short read alignment with Burrows-Wheeler transform. *Bioinformatics* 25, 1754–1760. [PubMed: 19451168]
- Liao Y, Smyth GK, and Shi W (2014). featureCounts: an efficient general purpose program for assigning sequence reads to genomic features. *Bioinformatics* 30, 923–930. [PubMed: 24227677]
- Linehan WM, Spellman PT, Ricketts CJ, Creighton CJ, Fei SS, Davis C, Wheeler DA, Murray BA, Schmidt L, Vocke CD, et al. ; Cancer Genome Atlas Research Network (2016). Comprehensive Molecular Characterization of Papillary Renal-Cell Carcinoma. *N. Engl. J. Med.* 374, 135–145. [PubMed: 26536169]
- Majzner RG, and Mackall CL (2019). Clinical lessons learned from the first leg of the CAR T cell journey. *Nat. Med.* 25, 1341–1355. [PubMed: 31501612]
- McDermott DF, Huseni MA, Atkins MB, Motzer RJ, Rini BI, Escudier B, Fong L, Joseph RW, Pal SK, Reeves JA, et al. (2018). Clinical activity and molecular correlates of response to atezolizumab alone or in combination with bevacizumab versus sunitinib in renal cell carcinoma. *Nat. Med.* 24, 749–757. [PubMed: 29867230]
- McKenna A, Hanna M, Banks E, Sivachenko A, Cibulskis K, Kernytsky A, Garimella K, Altshuler D, Gabriel S, Daly M, and DePristo MA (2010). The Genome Analysis Toolkit: a MapReduce framework for analyzing next-generation DNA sequencing data. *Genome Res.* 20, 1297–1303. [PubMed: 20644199]
- Mitchell TJ, Turajlic S, Rowan A, Nicol D, Farmery JHR, O'Brien T, Martincorena I, Tarpey P, Angelopoulos N, Yates LR, et al. (2018). Timing the Landmark Events in the Evolution of Clear Cell Renal Cell Cancer: TRACERx Renal. *Cell* 173, 611–623.e17. [PubMed: 29656891]
- Moch H, Cubilla AL, Humphrey PA, Reuter VE, and Ulbright TM (2016). The 2016 WHO classification of tumours of the urinary system and male genital organs—part A: renal, penile, and testicular tumours. *Eur. Urol.* 70, 93–105. [PubMed: 26935559]
- Moserle L, Pons R, Martínez-Lozano M, Jiménez-Valerio GA, Vidal A, Suárez C, Trilla E, Jiménez J, de Torres I, Carles J, et al. (2020). Kidney cancer PDOXs reveal patient-specific pro-malignant effects of antiangiogenics and its molecular traits. *EMBO Mol. Med.* 12, e11889. [PubMed: 33151035]
- Motzer RJ, Hutson TE, Tomczak P, Michaelson MD, Bukowski RM, Oudard S, Negrier S, Szczylik C, Pili R, Bjarnason GA, et al. (2009). Overall survival and updated results for sunitinib compared with interferon alfa in patients with metastatic renal cell carcinoma. *J. Clin. Oncol.* 27, 3584–3590. [PubMed: 19487381]
- Motzer RJ, Rini BI, McDermott DF, Arén Frontera O, Hammers HJ, Carducci MA, Salman P, Escudier B, Beuselinck B, Amin A, et al. ; CheckMate 214 investigators (2019). Nivolumab plus ipilimumab versus sunitinib in first-line treatment for advanced renal cell carcinoma: extended follow-up of efficacy and safety results from a randomised, controlled, phase 3 trial. *Lancet Oncol.* 20, 1370–1385. [PubMed: 31427204]
- Motzer RJ, Banchereau R, Hamidi H, Powles T, McDermott D, Atkins MB, Escudier B, Liu L-F, Leng N, Abbas AR, et al. (2020a). Molecular Subsets in Renal Cancer Determine Outcome to Checkpoint and Angiogenesis Blockade. *Cancer Cell* 38, 803–817.e4. [PubMed: 33157048]
- Motzer RJ, Robbins PB, Powles T, Albiges L, Haanen JB, Larkin J, Mu XJ, Ching KA, Uemura M, Pal SK, et al. (2020b). Avelumab plus axitinib versus sunitinib in advanced renal cell carcinoma:

- biomarker analysis of the phase 3 JAVELIN Renal 101 trial. *Nat. Med.* 26, 1733–1741. [PubMed: 32895571]
- Motzer R, Alekseev B, Rha S-Y, Porta C, Eto M, Powles T, Grünwald V, Hutson TE, Kopyltsov E, Meéndez-Vidal MJ, et al. ; CLEAR Trial Investigators (2021). Lenvatinib plus Pembrolizumab or Everolimus for Advanced Renal Cell Carcinoma. *N. Engl. J. Med.* 384, 1289–1300. [PubMed: 33616314]
- Mouw KW, Goldberg MS, Konstantinopoulos PA, and D’Andrea AD (2017). DNA Damage and Repair Biomarkers of Immunotherapy Response. *Cancer Discov.* 7, 675–693. [PubMed: 28630051]
- Mullen AR, Hu Z, Shi X, Jiang L, Boroughs LK, Kovacs Z, Boriack R, Rakheja D, Sullivan LB, Linehan WM, et al. (2014). Oxidation of alpha-ketoglutarate is required for reductive carboxylation in cancer cells with mitochondrial defects. *Cell Rep.* 7, 1679–1690. [PubMed: 24857658]
- Neumeister VM, and Juhl H (2018). Tumor Pre-Analytics in Molecular Pathology: Impact on Protein Expression and Analysis. *Curr. Pathobiol. Rep.* 6, 265–274. [PubMed: 30595971]
- Paluch-Shimon S, and Cardoso F (2021). PARP inhibitors coming of age. *Nat. Rev. Clin. Oncol.* 18, 69–70. [PubMed: 33239729]
- Panda A, de Cubas AA, Stein M, Riedlinger G, Kra J, Mayer T, Smith CC, Vincent BG, Serody JS, Beckermann KE, et al. (2018). Endogenous retrovirus expression is associated with response to immune checkpoint blockade in clear cell renal cell carcinoma. *JCI Insight* 3, e121522.
- Pavía-Jiménez A, Tcheuyap VT, and Brugarolas J (2014). Establishing a human renal cell carcinoma tumorgraft platform for preclinical drug testing. *Nat. Protoc.* 9, 1848–1859. [PubMed: 25010905]
- Peña-Llopis S, and Brugarolas J (2013). Simultaneous isolation of high-quality DNA, RNA, miRNA and proteins from tissues for genomic applications. *Nat. Protoc.* 8, 2240–2255. [PubMed: 24136348]
- Peña-Llopis S, Vega-Rubín-de-Celis S, Liao A, Leng N, Pavía-Jiménez A, Wang S, Yamasaki T, Zhebker L, Sivanand S, Spence P, et al. (2012). BAP1 loss defines a new class of renal cell carcinoma. *Nat. Genet.* 44, 751–759. [PubMed: 22683710]
- Powles T, Plimack ER, Soulières D, Waddell T, Stus V, Gafanov R, Nosov D, Pouliot F, Melichar B, Vynnychenko I, et al. (2020). Pembrolizumab plus axitinib versus sunitinib monotherapy as first-line treatment of advanced renal cell carcinoma (KEYNOTE-426): extended follow-up from a randomised, open-label, phase 3 trial. *Lancet Oncol.* 21, 1563–1573. [PubMed: 33284113]
- Ricketts CJ, De Cubas AA, Fan H, Smith CC, Lang M, Reznik E, Bowlby R, Gibb EA, Akbani R, Beroukhim R, et al. ; Cancer Genome Atlas Research Network (2018). The Cancer Genome Atlas Comprehensive Molecular Characterization of Renal Cell Carcinoma. *Cell Rep.* 23, 313–326.e5. [PubMed: 29617669]
- Scheuermann TH, Tomchick DR, Machius M, Guo Y, Bruick RK, and Gardner KH (2009). Artificial ligand binding within the HIF2alpha PAS-B domain of the HIF2 transcription factor. *Proc. Natl. Acad. Sci. USA* 106, 450–455. [PubMed: 19129502]
- Scheuermann JC, de Ayala Alonso AG, Oktaba K, Ly-Hartig N, McGinty RK, Fraterman S, Wilm M, Muir TW, and Müller J (2010). Histone H2A deubiquitinase activity of the Polycomb repressive complex PR-DUB. *Nature* 465, 243–247. [PubMed: 20436459]
- Scheuermann TH, Li Q, Ma H-W, Key J, Zhang L, Chen R, Garcia JA, Naidoo J, Longgood J, Frantz DE, et al. (2013). Allosteric inhibition of hypoxia inducible factor-2 with small molecules. *Nat. Chem. Biol.* 9, 271–276. [PubMed: 23434853]
- Sharma P, and Allison JP (2020). Dissecting the mechanisms of immune checkpoint therapy. *Nat. Rev. Immunol.* 20, 75–76. [PubMed: 31925406]
- Singla N, Xie Z, Zhang Z, Gao M, Yousuf Q, Onabolu O, McKenzie T, Tcheuyap VT, Ma Y, Choi J, et al. (2020). Pancreatic tropism of metastatic renal cell carcinoma. *JCI Insight* 5, e134564.
- Sivanand S, Peña-Llopis S, Zhao H, Kucejova B, Spence P, Pavía-Jiménez A, Yamasaki T, McBride DJ, Gillen J, Wolff NC, et al. (2012). A validated tumorgraft model reveals activity of dovitinib against renal cell carcinoma. *Sci. Transl. Med.* 4, 137ra75.

- Sobczuk P, Brodziak A, Khan MI, Chhabra S, Fiedorowicz M, Welniak-Kamińska M, Synoradzki K, Bartnik E, Cudnoch-Jędrzejewska A, and Czarnecka AM (2020). Choosing The Right Animal Model for Renal Cancer Research. *Transl. Oncol.* 13, 100745. [PubMed: 32092671]
- Sung H, Ferlay J, Siegel RL, Laversanne M, Soerjomataram I, Jemal A, and Bray F (2021). Global Cancer Statistics 2020: GLOBOCAN Estimates of Incidence and Mortality Worldwide for 36 Cancers in 185 Countries. *CA Cancer J. Clin.* 71, 209–249. [PubMed: 33538338]
- Tannir NM, Signoretti S, Choueiri TK, McDermott DF, Motzer RJ, Flaifel A, Pignon J-C, Ficial M, Frontera OA, George S, et al. (2021). Efficacy and Safety of Nivolumab Plus Ipilimumab versus Sunitinib in First-line Treatment of Patients with Advanced Sarcomatoid Renal Cell Carcinoma. *Clin. Cancer Res.* 27, 78–86. [PubMed: 32873572]
- Turajlic S, Xu H, Litchfield K, Rowan A, Chambers T, Lopez JI, Nicol D, O'Brien T, Larkin J, Horswell S, et al. ; PEACE; TRACERx Renal Consortium (2018a). Tracking Cancer Evolution Reveals Constrained Routes to Metastases: TRACERx Renal. *Cell* 173, 581–594.e12. [PubMed: 29656895]
- Turajlic S, Xu H, Litchfield K, Rowan A, Horswell S, Chambers T, O'Brien T, Lopez JI, Watkins TBK, Nicol D, et al. ; TRACERx Renal Consortium (2018b). Deterministic Evolutionary Trajectories Influence Primary Tumor Growth: TRACERx Renal. *Cell* 173, 595–610.e11. [PubMed: 29656894]
- Van der Auwera GA, Carneiro MO, Hartl C, Poplin R, Del Angel G, Levy-Moonshine A, Jordan T, Shakir K, Roazen D, Thibault J, et al. (2013). From FastQ data to high confidence variant calls: the Genome Analysis Toolkit best practices pipeline. *Curr. Protoc. Bioinformatics* 43, 11.10.1–11.10.33. [PubMed: 25431634]
- Varna M, Bousquet G, Ferreira I, Goulard M, El-Bouchtaoui M, Artus PM, Verine J, de Kerviler E, Hernandez L, Leboeuf C, et al. (2014). Stability of preclinical models of aggressive renal cell carcinomas. *Int. J. Clin. Exp. Pathol.* 7, 2950–2962. [PubMed: 25031714]
- Vento J, Mulgaonkar A, Woolford L, Nham K, Christie A, Bagrodia A, de Leon AD, Hannan R, Bowman I, McKay RM, et al. (2019). PD-L1 detection using <sup>89</sup>Zr-atezolizumab immuno-PET in renal cell carcinoma tumorgrafts from a patient with favorable nivolumab response. *J. Immunother. Cancer* 7, 144. [PubMed: 31155004]
- Vera-Badillo FE, Conde E, and Duran I (2012). Chromophobe renal cell carcinoma: a review of an uncommon entity. *Int. J. Urol.* 19, 894–900. [PubMed: 22715810]
- Vosjan MJ, Perk LR, Visser GW, Budde M, Jurek P, Kiefer GE, and van Dongen GA (2010). Conjugation and radiolabeling of monoclonal antibodies with zirconium-89 for PET imaging using the bifunctional chelate p-iso-thiocyanatobenzyl-desferrioxamine. *Nat. Protoc.* 5, 739–743. [PubMed: 20360768]
- Wallace EM, Rizzi JP, Han G, Wehn PM, Cao Z, Du X, Cheng T, Czerwinski RM, Dixon DD, Goggin BS, et al. (2016). A Small-Molecule Antagonist of HIF2α Is Efficacious in Preclinical Models of Renal Cell Carcinoma. *Cancer Res.* 76, 5491–5500. [PubMed: 27635045]
- Wang T, Lu R, Kapur P, Jaiswal BS, Hannan R, Zhang Z, Pedrosa I, Luke JJ, Zhang H, Goldstein LD, et al. (2018). An Empirical Approach Leveraging Tumorgrafts to Dissect the Tumor Microenvironment in Renal Cell Carcinoma Identifies Missing Link to Prognostic Inflammatory Factors. *Cancer Discov.* 8, 1142–1155. [PubMed: 29884728]
- Wertz IE, and Wang X (2019). From Discovery to Bedside: Targeting the Ubiquitin System. *Cell Chem. Biol.* 26, 156–177. [PubMed: 30554913]
- Wolff NC, Pavia-Jiménez A, Tcheuyap VT, Alexander S, Vishwanath M, Christie A, Xie X-J, Williams NS, Kapur P, Posner B, et al. (2015). High-throughput simultaneous screen and counterscreen identifies homoharringtonine as synthetic lethal with von Hippel-Lindau loss in renal cell carcinoma. *Oncotarget* 6, 16951–16962. [PubMed: 26219258]
- Zaman A, Wu W, and Bivona TG (2019). Targeting Oncogenic BRAF: Past, Present, and Future. *Cancers (Basel)* 11, 1197.
- Zhao H, Nolley R, Chan AMW, Rankin EB, and Peehl DM (2017). Cabozantinib inhibits tumor growth and metastasis of a patient-derived xenograft model of papillary renal cell carcinoma with MET mutation. *Cancer Biol. Ther.* 18, 863–871. [PubMed: 27715452]

### Highlights

- Generation of a large PDX library from a diverse population
- The PDX library is characterized by next-generation sequencing (exome and RNA-seq)
- Interactive tool for selecting TG lines representative of RCC molecular subtypes
- Precision diagnostics and therapeutic applications illustrated

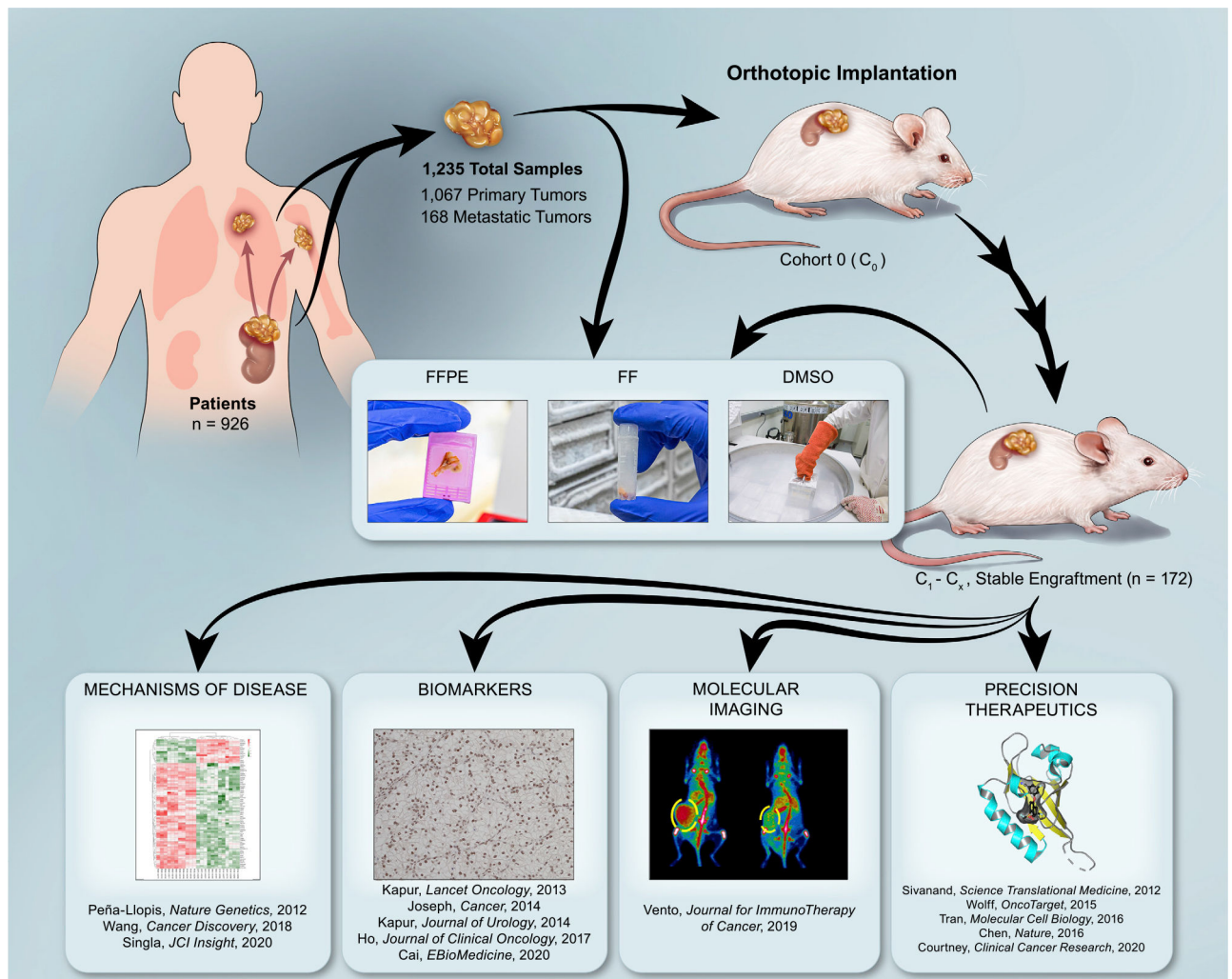


### Figure 1. UTSW KCP TG platform

Tumorgraft (TG) lines derived from primary tumors or metastases were generated through orthotopic implantation of additive-free fragments into the kidney of NOD/SCID mice. As the TGs grew, they were passaged into subsequent cohorts. Stable engraftment was defined as histologically confirmed tumor growth following passage through at least two cohorts of mice (i.e.,  $c_0$  and  $c_1$ ). Biobanking (formalin fixation and paraffin embedding [FFPE], flash freezing [FF], and DMSO cryopreservation) occurred at the time of initial tumor collection and following explantation of TG lines. This resource has broad applications ranging from exploration of tumor biology to development of novel therapies.

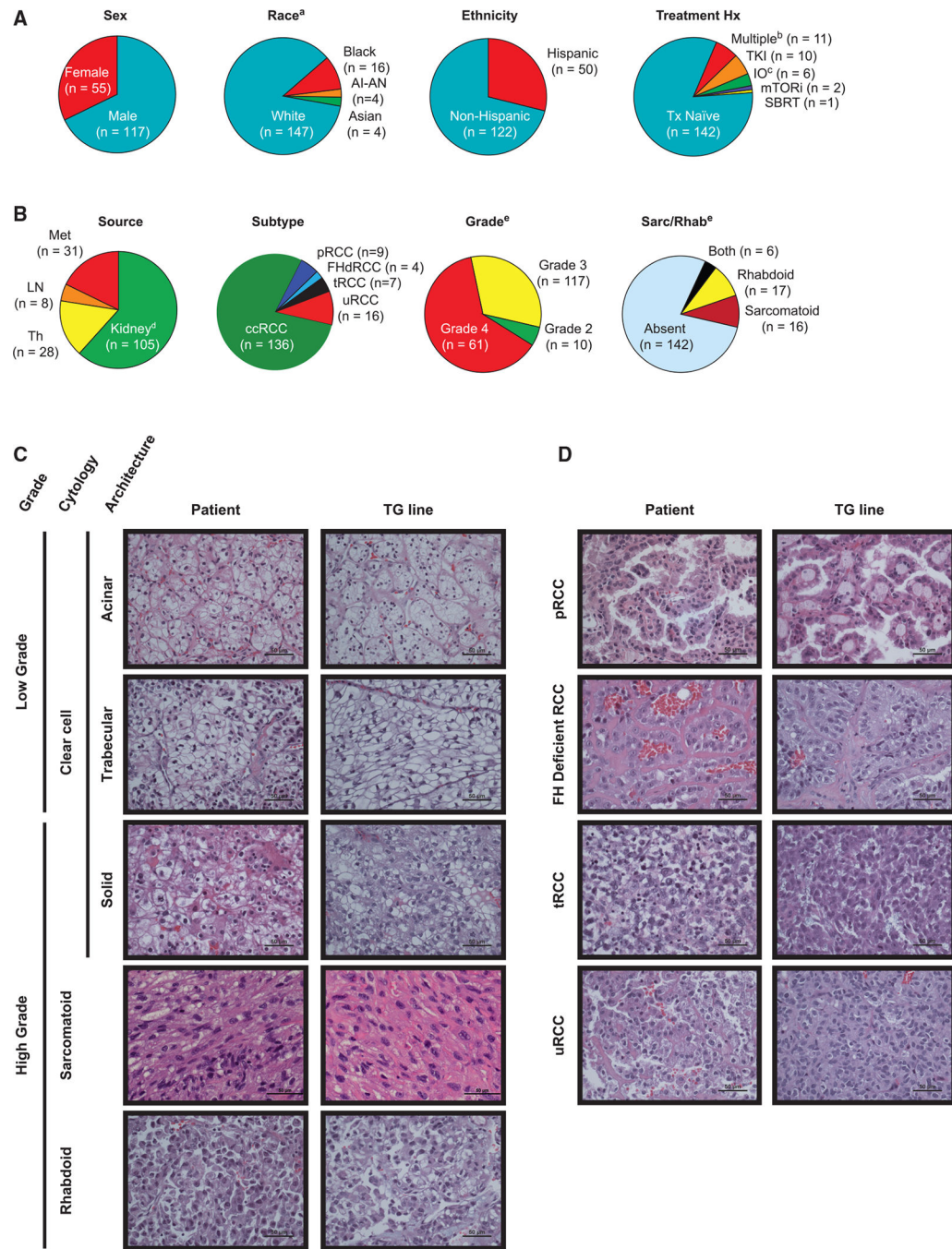


**Figure 2. Clinical and histological RCC diversity of the TG platform**

(A) Overview of the UTSW patients from whom the TG library was generated, including demographics and treatment history (prior to sample acquisition). An entry is included for each TG line, even when from the same individual (172 TG lines corresponding to 148 individuals). <sup>a</sup>Excludes one individual with unknown ethnicity. <sup>b</sup>Refers to multiple classes of therapies. <sup>c</sup>Includes both immune-checkpoint inhibitors as well as interleukin-2.

(B) Overview of tumor source, histological subtype, grade, and sarcomatoid/rhabdoid status (n = 172). <sup>d</sup>Includes two TG lines derived from direct invasion into the adrenal gland. <sup>e</sup>Totals are greater than 172 because of TG lines where multiple grades were noted.

(C and D) Comparative patient tumor and TG H&E sections demonstrating feature preservation in ccRCC (C) and nccRCC (D). AI-AN, American Indian/Alaskan Native; ccRCC, clear cell RCC; FhdRCC, FH-deficient RCC; IO, immune-oncology therapies; LN, lymph node; Met, metastasis; mTORi, mTOR inhibitors; pRCC, papillary RCC; Sarc/Rhab, sarcomatoid/rhabdoid; SBRT, stereotactic body radiotherapy; Th, tumor thrombus; TKI, tyrosine kinase inhibitor; tRCC, translocation RCC; Tx, treatment; uRCC, unclassified RCC.

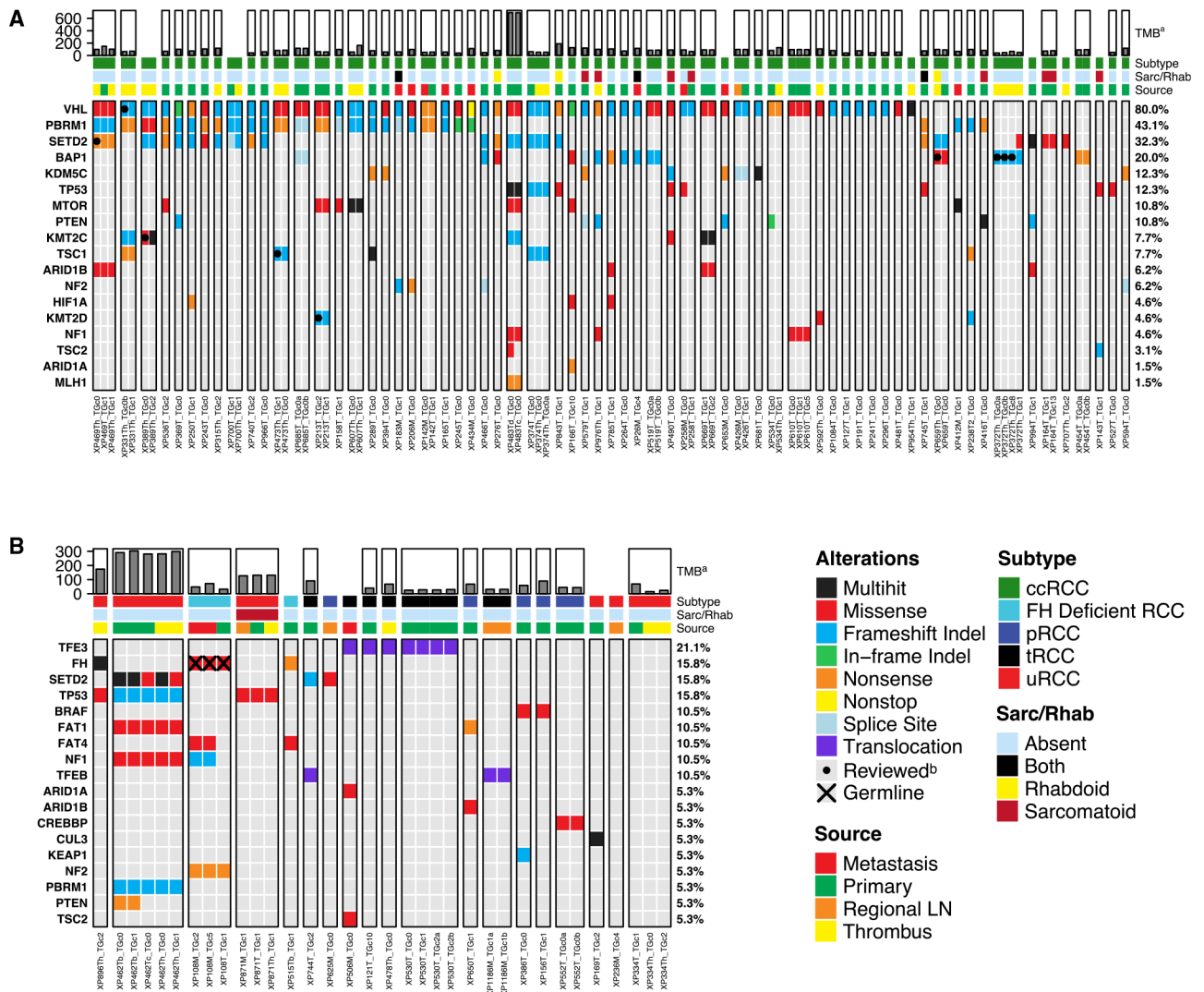


**Figure 3. Overview of driver mutations**  
 Integrated somatic mutation detection, germline mutation calling, and gene fusion data of 125 TG samples derived from (A) 65 individuals with ccRCC and (B) 19 with nccRCC. Samples originating from the same individual are grouped (Table S5). Percentages were calculated on a per-individual basis. <sup>a</sup>TMB was calculated as the sum of all putative somatic mutations for samples processed with a paired normal. A TMB value is not provided for tumors without a paired normal sample. <sup>b</sup>All paired samples with discordant mutational status were reviewed manually using the integrated genome viewer, and somatic mutations called via this method are annotated with a black dot.

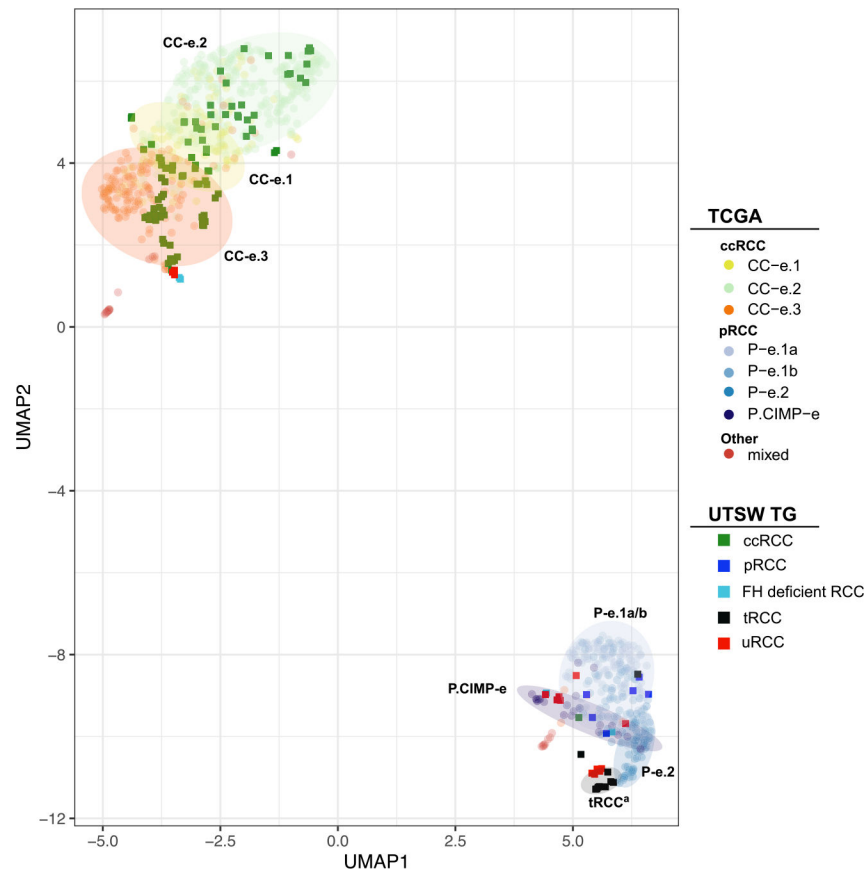


**Figure 4. Representation of molecularly defined RCC subtypes in the TG platform**

2D representation of samples according to  $\log_2$ -normalized gene expression values using the predefined TCGA gene signature after subtracting eTME genes (676 total genes) by UMAP. 131 samples from 102 unique TG lines (squares) and 817 reference samples from the TCGA cohort (circles) are included. chRCC TCGA samples ( $n = 77$ ) were filtered out. Reference clusters were predefined by previous TCGA allocation and used to map TGs into molecular clusters. <sup>a</sup>tRCC TG lines formed a distinct cluster (gray oval) that also included some uRCCs. A fully interactive version of this figure is also available (Data S1).

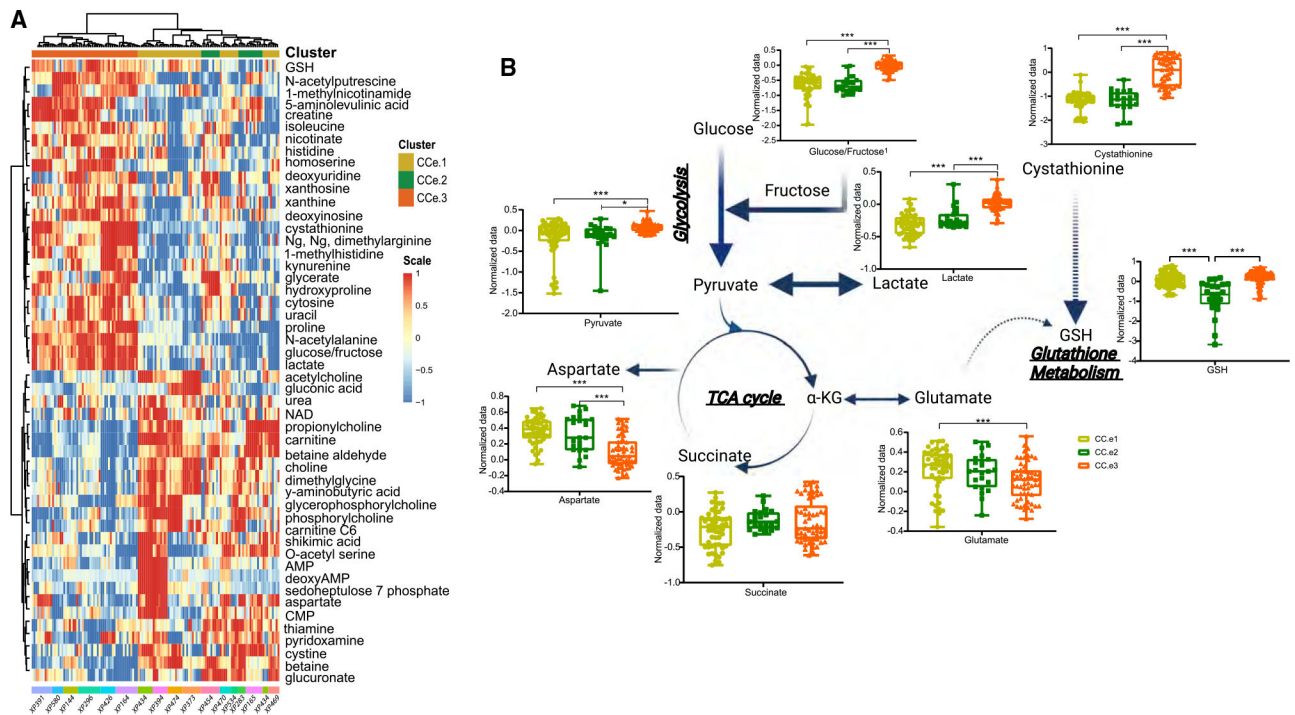


**Figure 5. Highlighted application: Exploring and probing metabolism**

(A) Unsupervised heatmap of the top 50 metabolites (false discovery rate [FDR]-corrected  $p < 0.05$ , one-way ANOVA) among ccRCC TG lines segregates CC-e.3 from CC-e.1 and CC-e.2 (clusters defined based on nearest neighbor transcriptomic analysis; Figure 4). Each line was processed with up to 2 biological replicates and at least 3 technical replicates for a total of 134 samples.

(B) Metabolic pathway map with metabolite quantitation showing increased glycolysis (glucose, lactate, and pyruvate) and cystathionine in the CC-e.3 subgroup relative to CC-e.1 and CC-e.2. Boxplots show relative abundance of metabolites in each cluster (normalized to the total ion count and  $\log_2$  transformed). Statistical significance was calculated using a mixed model with a compound symmetric covariance structure. \* $p < 0.05$ , \*\* $p < 0.01$ , \*\*\* $p < 0.001$ . Lower and upper limits of box plot represent 25th and 75th percentile, respectively. Error bars indicate 95% confidence interval.

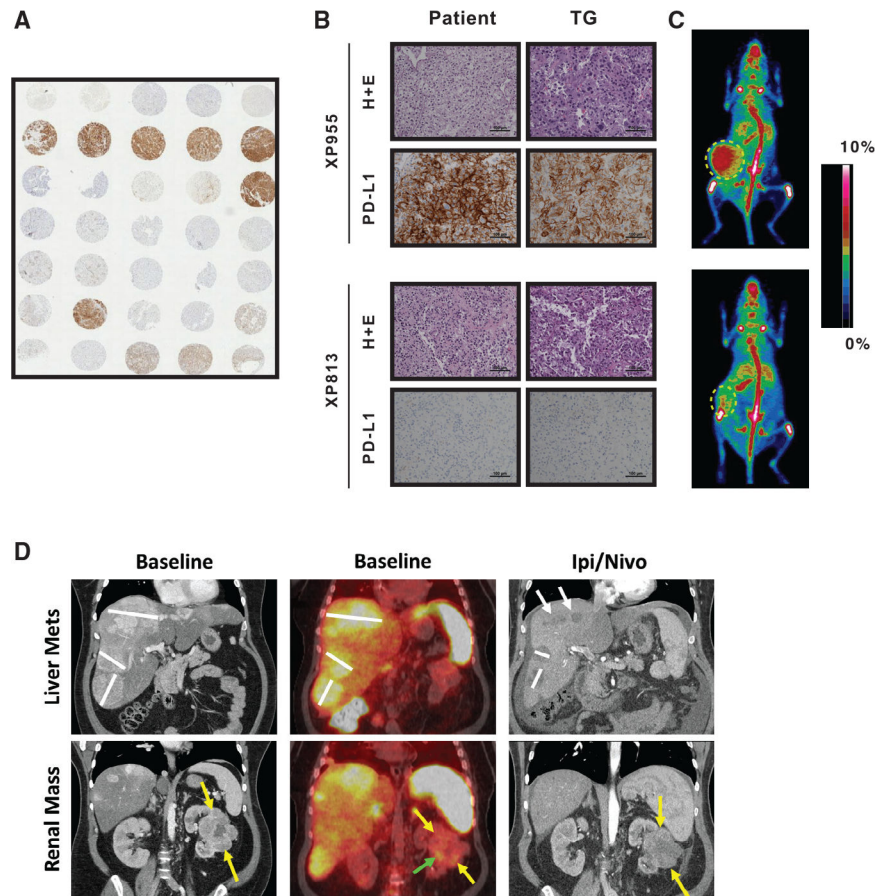


**Figure 6. Highlighted Application: Precision diagnostics**

(A) Representative tissue microarray of TG core biopsy samples stained with the PD-L1 antibody by IHC.

(B and C) Comparative H&E and PD-L1 IHC of tumors from affected individuals and corresponding TGs implanted subcutaneously into mice (white circle) with high (XP955) and low (XP813) PD-L1 expression with (C) representative  $^{89}\text{Zr}$ -ATZ PET images.

(D)  $^{89}\text{Zr}$ -ATZ PET/CT coronal images of an individual with metastatic ccRCC enrolled in the  $^{89}\text{Zr}$ -ATZ PET trial (NCT04006522) with accompanying pre- and post-ipilimumab/nivolumab (3 cycles) CT images showing early response of PD-L1-positive liver metastases (white lines and arrows) compared with PD-L1-negative primary tumor (yellow arrows) with minimal uptake (green arrow).

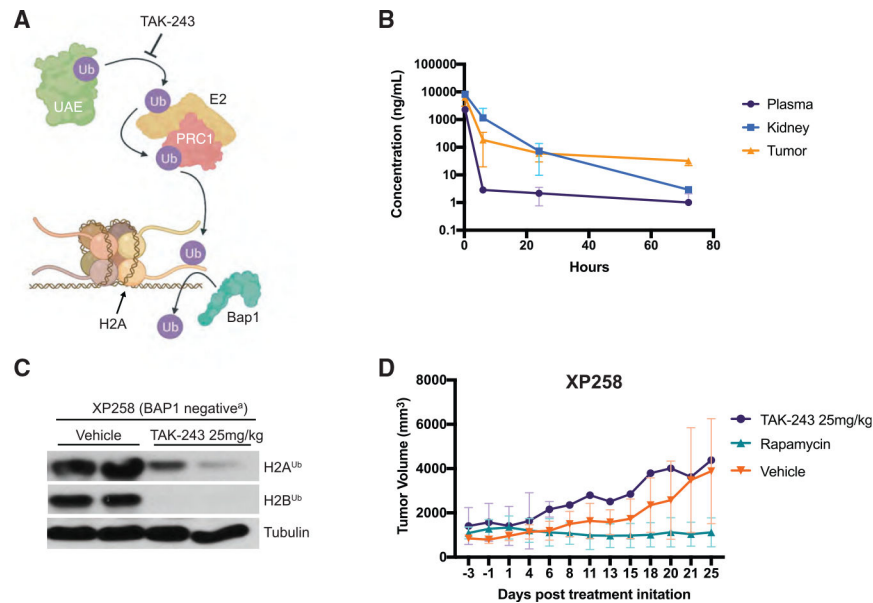


### Figure 7. Highlighted application: Precision therapy

(A) Rationale for targeting UAE in *BAP1*-deficient RCC. TAK-243 inhibits the ubiquitin-activating enzyme (UAE), which initiates the ubiquitination cascade. Downstream effects include histone H2AK119 ubiquitination, which is mediated by polycomb repressive complex 1 (PRC1) and leads to target gene silencing. BAP1, a histone deubiquitinase, acts on H2AK119ub.

(B) TAK-243 PK studies. 25 mg/kg of TAK-243 was administered i.v. into subcutaneous TG-bearing NOD/SCID mice (XP373). TAK-243 concentrations in plasma, kidneys, and TG were determined by sacrificing mice at 15 min (n = 3), 24 h (n = 3), 48 h (n = 3), and 72 h (n = 3). Data are mean  $\pm$  SD.

(C) Western blot analysis of TG from mice treated with TAK-243 or vehicle 48 h after injection. H2A<sup>Ub</sup> (Lys119) and H2B<sup>Ub</sup> (Lys120) immunoblots were performed on explanted tumors. <sup>a</sup>BAP1 loss in XP258 determined by IHC (Peña-Llopis et al., 2012).

(D) Tumor volumes from a BAP1-negative TG line (XP258) treated (starting at day 0) with TAK-243 (25 mg/kg i.v. every 72 h) (n = 3), vehicle (n = 3), or rapamycin (0.5 mg/kg intraperitoneally every 48 h) (n = 3). Data are means  $\pm$  SD.

## KEY RESOURCES TABLE

REAGENT or RESOURCE	SOURCE	IDENTIFIER
Antibodies		
Rabbit monoclonal PD-L1	Biocare Medical	CAT#: ACI3171A; RRID: AB_2747371
Rabbit monoclonal BAP1 (D7W7O)	Cell Signaling Technology	CAT#: 13271; RRID:AB_2798168
Rabbit monoclonal Ubiquityl-Histone H2A (D27C4)	Cell Signaling Technology	CAT#: 8240; RRID:AB_10891618
Rabbit monoclonal Ubiquityl-Histone H2B (D11)	Cell Signaling Technology	CAT#: 5546; RRID:AB_10693452
Biological samples		
Human kidney cancer tissues	UT Southwestern Kidney Cancer Program	<a href="https://www.utsouthwestern.edu/departments/kidney-cancer/">https://www.utsouthwestern.edu/departments/kidney-cancer/</a>
Patient-derived xenografts (PDXs)	This publication	N/A
Chemicals, peptides, and recombinant proteins		
TAK-243 (MLN7243) UAE inhibitor	Chemietek	CAT#: 1450833-55-2
Rapamycin	LC Laboratories	CAT#: R5000
Yttrium foil	Alfa Aesar	CAT#: 00616
Chelex-100 Chelating Resin	Bio-Rad Laboratories	CAT#: 1422832
Accell PLUS CM Resin	Waters	CAT#: WAT010740
Oxalic acid, anhydrous	Sigma-Aldrich	CAT#: 75688
Hydroxylamine hydrochloride, trace metals basis	Sigma-Aldrich	CAT#: 431362
2,3,5,6-Tetrafluorophenol, 98%	Acros Organics	CAT#: 188390050
Atezolizumab (ATZ)	Genentech/Roche	N/A
p-SCN-Bn-Deferoxamine	Macrocyclics	CAT#: B-705
Amicon Ultra-4 Centrifugal filters, 50K MWCO	EMD Millipore	CAT#: UFC805024
Zeba™ Spin Desalting Columns, 40K MWCO	Pierce Biotechnology	CAT#: 87771
Critical commercial assays		
AllPrep DNA/RNA Micro Kit	QIAGEN	CAT#: 80204
Deposited data		
WES and RNaseq raw data	This publication. EGA: EGAS00001005516	<a href="https://ega-archive.org/studies/EGAS00001005516">https://ega-archive.org/studies/EGAS00001005516</a>
eFIG4	This publication	N/A
Experimental models: Organisms/strains		
NOD.CB17-Prkdc <sup>scid</sup> (NOD/SCID) mice	UTSW Breeding Core	N/A
Software and algorithms		

REAGENT or RESOURCE	SOURCE	IDENTIFIER
BWA-MEM	Li and Durbin, 2009	<a href="https://github.com/lh3/bwa">https://github.com/lh3/bwa</a>
Samtools	Danecek et al., 2021	<a href="http://www.htslib.org/">http://www.htslib.org/</a>
Picard	Broad Institute	<a href="https://broadinstitute.github.io/picard">https://broadinstitute.github.io/picard</a>
GATK	Broad Institute	<a href="https://gatk.broadinstitute.org/hc/en-us">https://gatk.broadinstitute.org/hc/en-us</a>
Mouse read filtration and human aligned mouse alleles	Jo et al., 2019	<a href="https://github.com/Yonsei-TGIL/BestPractice_for_PDMseq">https://github.com/Yonsei-TGIL/BestPractice_for_PDMseq</a>
MuTect2	Cibulskis et al., 2013	<a href="https://gatk.broadinstitute.org/hc/en-us/articles/360037593851-Mutect2">https://gatk.broadinstitute.org/hc/en-us/articles/360037593851-Mutect2</a>
FreeBayes	Garrison and Marth, 2012	<a href="https://github.com/freebayes/freebayes">https://github.com/freebayes/freebayes</a>
Strelka2	Kim et al., 2018	<a href="https://github.com/Illumina/strelka">https://github.com/Illumina/strelka</a>
VCF2MAF	MSKCC	<a href="https://github.com/mskcc/vcf2maf">https://github.com/mskcc/vcf2maf</a>
hisat2	Kim et al., 2019	<a href="http://daehwankimlab.github.io/hisat2/">http://daehwankimlab.github.io/hisat2/</a>
ComplexHeatmap	Gu et al., 2016	<a href="https://github.com/jokergoo/ComplexHeatmap">https://github.com/jokergoo/ComplexHeatmap</a>
SVA	Bioconductor	<a href="https://bioconductor.org/packages/release/bioc/html/sva.html">https://bioconductor.org/packages/release/bioc/html/sva.html</a>
umap	<a href="https://cran.r-project.org">R-project.org</a>	<a href="https://cran.r-project.org/web/packages/umap">https://cran.r-project.org/web/packages/umap</a>
MultiQuant v2.1	SCIEX	
MetaboAnalyst v4.0	Chong et al., 2019	<a href="https://www.metaboanalyst.ca/MetaboAnalyst/home.xhtml">https://www.metaboanalyst.ca/MetaboAnalyst/home.xhtml</a>
Other		
eTME Gene Signature	Wang et al., 2018	<a href="https://lce.biohpc.swmed.edu/dishet/">https://lce.biohpc.swmed.edu/dishet/</a>
TCGA KIPAN gene signature	Chen et al., 2016a	Table S2